
HINOTORI I: The Nature of Rejuvenation Galaxies

Takumi S. TANAKA^{1,2,3*}, **Kazuhiro SHIMASAKU**^{1,4}, **Sandro TACCHELLA**^{5,6},
Makoto ANDO¹, **Kei ITO**¹, **Hassen M. YESUF**^{2,7} and **Suin MATSUI**¹

¹Department of Astronomy, Graduate School of Science, The University of Tokyo, 7-3-1 Hongo, Bunkyo-ku, Tokyo 113-0033, Japan

²Kavli Institute for the Physics and Mathematics of the Universe, The University of Tokyo, Kashiwa, Chiba 277-8583, Japan

³Center for Data-Driven Discovery, Kavli IPMU (WPI), UTIAS, The University of Tokyo, Kashiwa, Chiba 277-8583, Japan

⁴Research Center for the Early Universe, Graduate School of Science, The University of Tokyo, 7-3-1 Hongo, Bunkyo-ku, Tokyo 113-0033, Japan

⁵Kavli Institute for Cosmology, University of Cambridge, Madingley Road, Cambridge CB3 0HA, UK

⁶Cavendish Laboratory, University of Cambridge, 19 JJ Thomson Avenue, Cambridge CB3 0HE, UK

⁷Kavli Institute for Astronomy and Astrophysics, Peking University, Beijing 100871, People's Republic of China

*E-mail: takumi.tanaka@ipmu.jp

Received ; Accepted

Abstract

We present the HINOTORI (star formation History INvestigatiOn TO find RejuvenatIon) project to reveal the nature of rejuvenation galaxies (RGs), which are galaxies that restarted their star formation after being quiescent. As the first step of HINOTORI, we construct the largest RG sample with 1071 sources. We select these RGs from 8857 MaNGA (Mapping Nearby Galaxies at APO) survey galaxies by reconstructing their star formation histories with PROSPECTOR spectral energy distribution fitting code. Both optical spectral data and UV to IR photometric data are used for the fitting. Using mock data, we confirm that our method can detect weak rejuvenation events that form only about 0.1% of the total stellar mass with high completeness. The RGs account for $\sim 10\%$ of the whole sample, and rejuvenation events contribute on average only about 0.1% of the total stellar mass in those galaxies but 17% of the cosmic-star formation rate density today. Our RGs have a similar mass distribution to quiescent galaxies (QGs). However, the morphology of the RGs is more disk-like than QGs, suggesting that rejuvenation may occur selectively in disk-like QGs. Our results also suggest the possibility of multiple-time rejuvenation events in a single galaxy. Further spatially resolved analyses of integral field unit data and radio observations and comparisons to simulations are needed to identify the mechanism and the role of rejuvenation in galaxy evolution.

Key words: galaxies: evolution — galaxies: star formation — galaxies: stellar content

1 Introduction

Galaxies segregate into two distinct groups in the star-formation rate (SFR) - stellar mass (M^*) diagram: “star-forming galaxies” (SFGs) with active star formation and “quiescent galaxies” (QGs) with low-to-no star formation (e.g., Renzini et al. 2015; Feldmann 2017). Because the fraction of QGs increases with cosmic time (e.g., Ilbert et al. 2013; Muzzin et al. 2013; Davidzon et al. 2017; Weaver et al. 2022), a widely-accepted simple galaxy evolution scenario is that SFGs stop star formation (quenching) and become QGs (e.g., Faber et al. 2007; Peng et al. 2010). Galaxies in between SFGs and QGs are called “green valley” galaxies (GVs). GVs are widely thought to be galaxies in transition from SFGs to QGs (e.g., Salim 2014; Angho et al. 2020).

Recent progress in the spectral energy distribution (SED) fitting technique (Walcher et al. 2011 for review) has enabled us to search for and analyze galaxies with unique star-formation histories (SFHs), such as “rejuvenating galaxies”, which have been overlooked in previous studies. Rejuvenating galaxies have resumed their star formation after being quiescent (e.g., Trayford et al. 2016; Cleland and McGee 2021; Zhang et al. 2022). We may need to update the simple evolution scenario from SFGs to QGs to explain rejuvenating galaxies.

Some studies (e.g., Chauke et al. 2019; Mancini et al. 2019; Tacchella et al. 2022) have also focused on “rejuvenated galaxies”. The difference between “rejuvenating galaxies” and “rejuvenated galaxies” is that the latter have terminated their resumed star-formation and have been quiescent again. Since both populations have experienced rejuvenation events, this paper deals with both populations and collectively refers to them as “rejuvenation galaxies” (RGs). We do not use the abbreviation “RG” when distinguishing between “rejuvenated galaxies” and “rejuvenating galaxies”.

RGs have been studied since the 2000s. Early studies, which are limited to the low- z universe, have selected early-type galaxies (ETGs) with recent star formation as RGs by using UV detection (Kaviraj et al. 2007; Donas et al. 2007; Schawinski et al. 2007), spectral and photometric features (Treu et al. 2005; Cleland and McGee 2021), or a stellar population synthesis (Thomas et al. 2010). The fraction of RGs (or ETGs with recent star formation) in previous samples ranges from 10% to 30% depending on the selection method and the properties of the parent samples. Recent developments in SED fitting methods and spectroscopic surveys in the intermediate- z universe enabled selecting $0.6 \lesssim z \lesssim 2$ RGs based on their SFHs or stellar ages reconstructed by SED fitting (Belli et al. 2017; Gobat et al.

2017; Carnall et al. 2019; Chauke et al. 2019; Mancini et al. 2019; Akhshik et al. 2021; Tacchella et al. 2022; Paspaliaris et al. 2023).

The mechanism and cause of rejuvenation and the role of rejuvenation in galaxy evolution are major open questions. On the cause of rejuvenation, some studies have suggested that rejuvenation is related to mergers. For example, Kaviraj et al. (2009) have used a simulation to show that a minor merger can explain the recent star formation of ETGs. Other studies have also suggested that gas accretion onto elliptical galaxies after merging may cause rejuvenation and enables rejuvenated ellipticals to acquire a disk and turn into red spirals or S0 galaxies (e.g., Mapelli et al. 2015; Diaz et al. 2018; Hao et al. 2019; Rathore et al. 2022). Paspaliaris et al. (2023) have argued that HI gas, as found in some ETGs by Thom et al. (2012), could cause rejuvenation. Note, however, that Park et al. (2022) have suggested that red disk-like QGs cannot be described with the above merger-rejuvenation scenario. Besides, Martin-Navarro et al. (2022) have reported that many type-I active galactic nuclei (AGN) had experienced rejuvenation, suggesting the relationship between rejuvenation events and AGN activities.

Understanding the rejuvenation mechanism will deepen our knowledge of the star formation activity in a galaxy. In particular, we can consider RGs as former QGs that could not maintain a quiescent state. Comparing RGs with QGs enables us to discuss the quenching process, especially the conditions needed to maintain a quiescent state.

The role of rejuvenation in galaxy evolution also remains to be evaluated. Chauke et al. (2019) and Tacchella et al. (2022) have reported that, at most, only about 10% of the total mass is formed in a rejuvenation event. However, we can detect only recent rejuvenation events because the time resolution of the reconstructed star formation history of a galaxy decreases with look-back time. Thus, we may underestimate the contributions of rejuvenation events to the total star-formation activities. The relationship between RGs and GVs is also relevant to the role of rejuvenation. GVs are widely thought to be in the quenching phase. However, this simple view needs to be modified if a significant fraction of GVs are RGs. Furthermore, Mancini et al. (2019) reported that the bending of the star-forming main sequence (SFMS) in the high-mass end is caused by RGs.

Despite the importance of RGs, previous studies have failed to discuss the nature of RGs statistically. This is mainly because the previous studies are based on either small samples of RGs or biased parent samples (e.g., RGs are selected from only QGs). For example, Tacchella et al. (2022) have found that RGs reside in massive dark ha-

los based on nine RGs selected from 161 QGs. Cleland and McGee (2021) have detected no significant environmental dependence of rejuvenation fraction in a sample of $\simeq 350$ RGs. However, these results need to be confirmed with a larger RG sample and with a more inclusive parent sample not limited to QGs. In addition, different definitions of RGs among the previous studies have also made it difficult to compare their results with each other and to compare them with simulation results (e.g., Kaviraj et al. 2009; Trayford et al. 2016; Pandya et al. 2017; Nelson et al. 2018; Behroozi et al. 2019; Alarcon et al. 2022).

We launch the HINOTORI¹ project to solve those problems. HINOTORI aims to understand the nature of RGs using well-constrained SFHs. Selecting RGs with reliable SFHs is the most direct selection method. As the first step of HINOTORI, we select RGs from a large ($N \sim 10^4$) parent sample of $z \simeq 0$ galaxies covering all morphological types. To reconstruct the SFH for individual galaxies, we run the Bayesian SED fitting library PROSPECTOR (Leja et al. 2017; Johnson et al. 2021) on their spectroscopic and UV to MIR photometric data. In this paper, we present the most extensive catalog to date of SFH-selected RGs and make the first secure statistical analysis of RGs.

Section 2 describes the data and how to make the input data for PROSPECTOR. Section 3 describes the SED fitting method and the selection method of RGs. In Sections 4 and 5, we show the results from a mock sample and real data, respectively. We discuss the nature of RGs in Section 6 and present a conclusion and prospects for future RG studies in Section 7. Throughout this work, we assume the cosmological parameters from the WMAP-9 (Hinshaw et al. 2013).

2 Data

2.1 MaNGA survey

We construct a parent sample from the sample of the MaNGA survey (Bundy et al. 2015), an integral field unit survey in the SDSS-IV (Blanton et al. 2017). This survey was carried out with the SDSS 2.5-meter telescope (Gunn et al. 2006) equipped with a fiber feed system (Drory et al. 2015) and the Baryon Oscillation Spectroscopic Survey (BOSS) spectrograph (Smee et al. 2013) covering 3600 – 10300 Å at $R \sim 2200$. The target galaxies of the MaNGA survey were selected from the NASA-Sloan atlas (NSA v1.0.1). See Yan et al. (2016) for the survey design. As detailed in Wake et al. (2017), the MaNGA sample consists of the following three samples selected with redshifts,

magnitudes, and colors to achieve a uniform number density distribution of M_i and additional targets selected for specific sciences.

- **Primary Sample:** Galaxies whose $1.5R_e$ area is covered by the IFU.
- **Secondary Sample:** Galaxies whose $2.5R_e$ area is covered by the IFU.
- **Color-Enhanced Sample:** Selected to fill in the region on the $\text{NUV} - i$ versus M_i color-magnitude diagram poorly sampled in the Primary and Secondary Samples. Galaxies in this region include low-luminosity red galaxies, high-luminosity blue galaxies, and GV. The IFU covers their $1.5R_e$, the same as the Primary Sample. The Primary Sample and the Color-Enhanced Sample are combined as the Primary+ Sample.
- **Ancillary Targets**²: Additionally selected 977 targets, such as luminous AGN, galaxies in voids, pairs and mergers, dwarf galaxies, blight cluster galaxies, and so on.

These galaxies are distributed over $5 \times 10^8 \leq M^*/M_\odot \leq 3 \times 10^{11}$ at $0.01 \leq z \leq 0.15$. In this study, we use the IFU data of 11,273 datacubes in the SDSS DR17 (Abdurro'uf et al. 2022) reduced with the version 3.1.1 MaNGA Data Reduction Pipeline (DRP: Law et al. 2016; Law et al. 2021), which performs flux calibration, sky subtraction, correction of the Galactic dust attenuation, and coadding individual exposures to make the final 3D datacubes of each galaxy.

Assuming that the RG fraction, the number ratio of RGs to total galaxies, is $f_{\text{RG}} \sim 10\%$ as suggested by Nelson et al. (2018); Behroozi et al. (2019); Chauke et al. (2019); Tacchella et al. (2022), we expect that the entire MaNGA sample includes $N \sim 10^3$ RGs, enabling a reliable statistical analysis. Besides, because all selected RGs have IFU spectroscopic data, we can also analyze the rejuvenation mechanism with spatially resolved characteristics.

2.2 Removing AGN, mergers, and pair galaxies

In this study, we do not use galaxies hosting active galactic nuclei (AGN) because PROSPECTOR has no AGN template other than dust torus emission in IR wavelengths (Leja et al. 2018). Comerford et al. (2020) published an AGN catalog selected from the 8th MaNGA Product Launch (MPL-8) sample. However, since this sample ($N = 6261$ galaxies) is smaller than the DR17 sample we use, we extend the selection method used by Comerford et al. (2020) to the DR17 MaNGA sample to exclude AGN. In total, we

¹ star-formation History INvestigatiON TO find RejuvenatIOn. Hinotori means phoenix in Japanese.

² <https://www.sdss4.org/dr17/manga/manga-target-selection/ancillary-targets/>

remove 406 AGN from the whole sample.

Merger and pair galaxies are also excluded using the `MANGA_TARGET3` information, a flag for ancillary targets, because it is difficult to create a 1D spectrum of a target galaxy by subtracting the contribution from its companion(s) in the 1D-flattening process described in section 2.4. We remove 119 galaxies that have either `TARGET3_PAIR_SIM`, `TARGET3_PAIR_RECENTER`, `TARGET3_PAIR_2IFU`, or `TARGET3_PAIR_ENLARGE` flag.

2.3 Crossmatching with photometric catalogs

For SED fitting, we use both photometric data from UV to MIR and IFU-flattened 1D spectroscopic data (see Section 2.4) to obtain more accurate SFHs than the existing SED fitting results, such as Pipe3D (Sánchez et al. 2016a; Sánchez et al. 2016b; Sánchez et al. 2018) and FIREFLY (Goddard et al. 2017; Parikh et al. 2018). For UV (FUV and NUV) photometry from Galaxy Evolution Explorer (GALEX) and optical (*ugriz*) photometry from the SDSS DR8, we use Sérsic fluxes summarized in the NSA and correct them for Galactic extinction using Schlegel et al. (1998). We also use IR photometry (W1, W2, W3, and W4) from the unWISE catalog (Schlafly et al. 2019), which is deeper than the ALLWISE catalog due to using coadd images and a forced photometry method (Lang et al. 2016). Furthermore, because the forced photometry is based on galaxy positions and profiles from the SDSS, the unWISE photometry is more consistent with the NSA photometry described above. By crossmatching MaNGA galaxies with the unWISE catalog with a maximum separation of 10 arcsec, we select 8857 sources with valid photometry (i.e., without missing values) as the main parent sample. The S/N distribution for each band and the redshift distribution of the sample are shown in figure 1. We find that crossmatching with the unWISE catalog does not affect the redshift distribution significantly.

2.4 1D flattening of datacubes

To transform 3D IFU data (with two spatial and one spectral dimensions) into a form that can be used for SED fitting, for each galaxy, we sum the spectra of all spatial positions to create a 1D spectrum in the following manner.

First, based on `MANGA_DRP3PIXMASK` information, we exclude invalid data with `FORESTAR` or `DONOTUSE` mask. `FORESTAR` means that the spaxel is contaminated by a foreground star while `DONOTUSE` means that the data of the spaxel are unreliable for some reason. We do not use a spaxel if it has even one wavelength bin masked with either flag. The `mask_1` panel in figure 2 shows the positions

removed by this operation in dark blue, and the `mask_2` panel shows the wavelengths removed by this operation (the value of 0 indicates that the wavelength has been removed).

Then, we remove spaxels that either have an invalid value at least one wavelength bin or are located near the edge of the field of view, i.e., at a distance from the center being greater than 0.8 times the maximum distance of all spaxels. The locations removed by this operation are shown in dark blue in figure 2, `mask_3`.

In addition, we mask three wavelength ranges [5500 Å, 5600 Å], [5850 Å, 5950 Å], and [6250 Å, 6450 Å] because luminous airglow emission lines contaminate. These wavelength ranges are shown in dark gray in the spectral and S/N wavelength dependence diagrams in figure 2.

Finally, we coadd the spaxels not masked by the above operations to produce 1D-spectrum data. We calculate the errors in 1D spectra by assuming a normal distribution of errors for each spaxel. An example coadded 1D-spectrum and its S/N are shown in the second and third lines in figure 2.

As mentioned in section 2.1, the size of the MaNGA field of view varies depending on the sample type. The field of view covers $1.5R_e$ for the Primary Sample and $2.5R_e$ for the Secondary Sample, where R_e is the effective radius. However, we do not perform aperture correction according to sample type. This is because PROSPECTOR has the function of photospectral correction as explained in section 3.1.2. Note that if there is non-negligible radial dependence in spectra, e.g., strong star formation only outside $1.5R_e$, there may be a bias between the Primary Sample and the Secondary Sample.

2.5 Value-added catalogs

The MaNGA sample has various value-added catalogs³ (VAC). Another advantage of using MaNGA data set is those VACs, and we can discuss the characteristics of RGs in more detail and more easily with such catalogs.

In this study, we use two VACs. First, we use “MaNGA PyMorph DR17 photometric catalog” (Domínguez Sánchez et al. 2022) in section 5.4 to discuss the morphology of the selected RGs. Second, we use “MaNGA Pipe3D value-added catalog: Spatially resolved and integrated properties of galaxies for DR17” (Pipe3D, Sánchez et al. 2022) in appendix to validate the results of our SED fitting. We describe the detail of each catalog and the used values in the individual sections.

³ https://www.sdss4.org/dr17/data_access/value-added-catalogs/

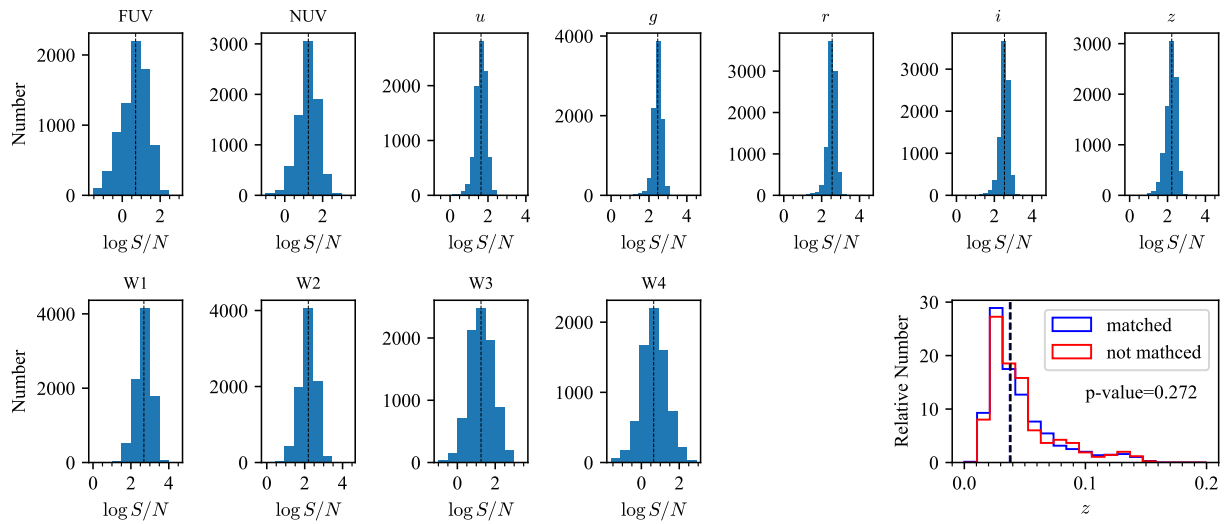


Fig. 1. Summary of the photometry of the main parent sample. Histograms show the $\log S/N$ distribution of our sample in each photometric band. The first row represents FUV, NUV, u , g , r , i , and z , respectively, from left to right. The second row represents W1, W2, W3, and W4, respectively, from left to right. The median S/N value is shown at the top of each panel. The bottom right panel shows the redshift distribution. The blue line shows the distribution of MaNGA galaxies matched with the unWISE catalog, i.e., our parent sample, while the red line shows the distribution of MaNGA galaxies not matched with the unWISE catalog. The p-value from the Kolmogorov–Smirnov (KS) test is shown in the panel.

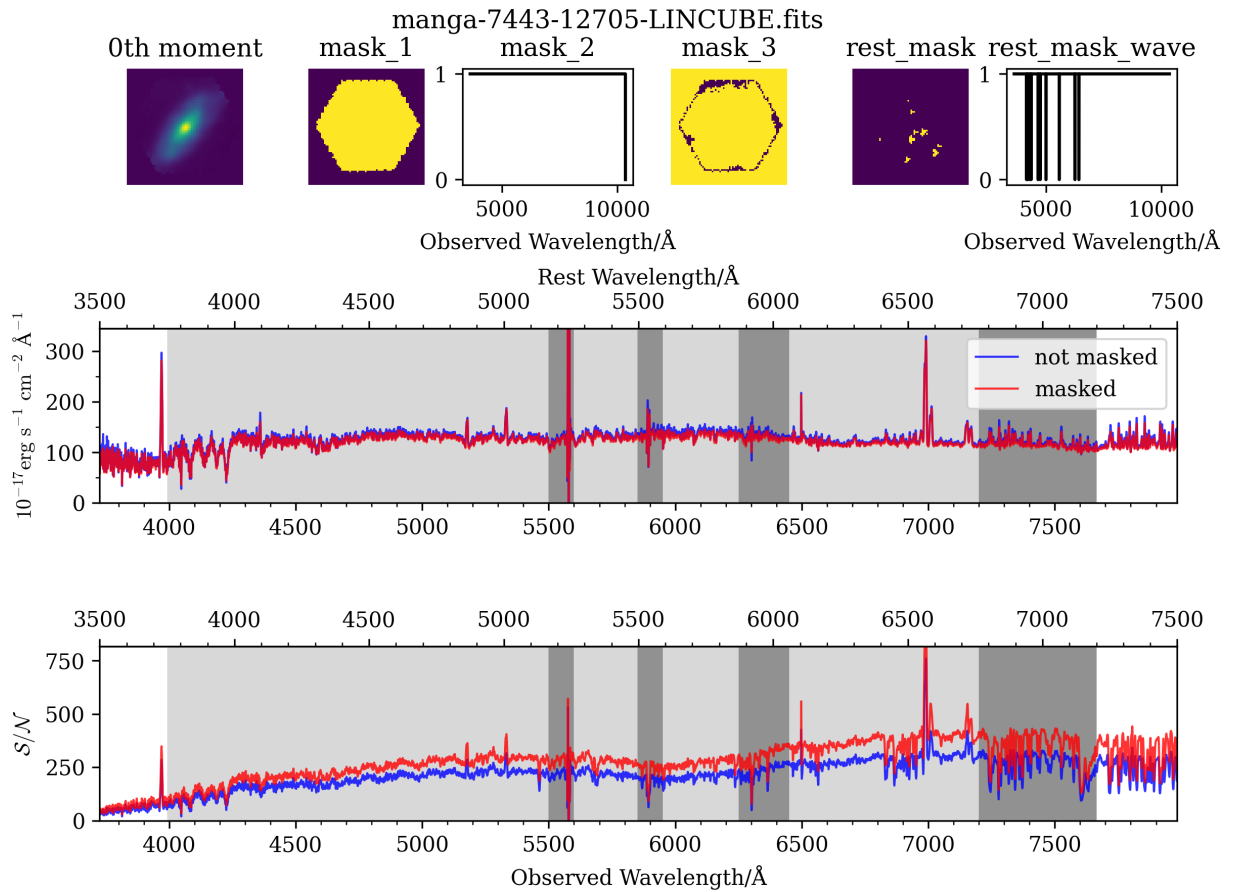


Fig. 2. An example of our 1D flattening procedure. The first row shows the 0th moment of an example galaxy and the distributions of masks used in the 1D-flattening procedure. The second and third rows show a coadded 1D spectrum and its S/N distribution, respectively, with the red (blue) line indicating the result with (without) masking.

3 Methodology

3.1 SED fitting

SED fitting is a technique of fitting observed data (photometry and/or spectroscopy) with model spectra (for a review, see Walcher et al. 2011). Through SED fitting, we can estimate basic parameters of galaxies such as stellar mass (M^*), dust attenuation (τ), and star formation history (SFH).

3.1.1 PROSPECTOR

PROSPECTOR (Leja et al. 2017; Johnson et al. 2021) is a Bayesian-based SED fitting code with which it is possible to fit with a flexible non-parametric SFH (e.g., Cid Fernandes et al. 2005; Ocvirk et al. 2006; Tojeiro et al. 2007; Dye 2008) by dividing look-back time into several age bins and assuming a constant SFR in each bin.

With high-quality input data, non-parametric SFH fitting can reproduce the true SFH more accurately than parametric SFH methods because of fewer assumptions on the SFH (e.g., Leja et al. 2019). Lower et al. (2020) have suggested that a non-parametric SFH can also estimate M^* more accurately. However, we should note that non-parametric SFH estimation still has prior dependence as Leja et al. (2019) have demonstrated. PROSPECTOR can fit spectroscopic and photometric data together to constrain parameters more tightly than fitting only photometric data (Johnson et al. 2021).

In this study, we input a flattened 1D spectrum and photometric data of each galaxy to PROSPECTOR and estimate a non-parametric SFH to select RGs. Below we briefly describe our parameter setting (for a detailed description of PROSPECTOR, see Leja et al. 2017; Johnson et al. 2021).

3.1.2 PROSPECTOR settings

Stellar population: PROSPECTOR uses the Flexible Stellar Population Synthesis (FSPS, Conroy et al. 2009; Conroy and Gunn 2010) to generate model SEDs of galaxies. We assume a Chabrier (2003) initial mass function. We set stellar metallicity, total stellar mass, and the velocity dispersion of stellar components as free parameters and assume that their priors are uniform in $\log(Z^*/Z_\odot)$ between -2 and 0.19 , in $\log(M^*/M_\odot)$ between 10^8 and 10^{13} , and uniform between 10 km/s and 300 km/s.

Nebular emission: We use nebular emission templates in PROSPECTOR that are based on CLOUDY (Ferland et al. 1998; Ferland et al. 2013) and described in Byler et al. (2017). We assume that gas-phase metallicity is equal to stellar metallicity. We set the ionization parameter $\log U$ as a free parameter with a uniform prior

between -4 and -1 .

Dust emission: We also use dust emission templates with fixed parameters. We do not use AGN dust emission templates because we have excluded AGN-hosting galaxies in the sample selection (section 2.2).

Dust attenuation: We assume the two-component dust attenuation model by Charlot and Fall (2000). This model has two types of attenuation. One is the attenuation only for birth clouds, $\tau_{\text{dust},1}(\lambda)$, calculated as:

$$\tau_{\text{dust},1}(\lambda) = \hat{\tau}_{\text{dust},1} \left(\frac{\lambda}{5500 \text{ \AA}} \right)^{-1}. \quad (1)$$

The other is the attenuation for the entire galaxy, $\tau_{\text{dust},2}(\lambda)$. We use the equation of Noll et al. (2009):

$$\tau_{\text{dust},2}(\lambda) = \hat{\tau}_{\text{dust},2} (k(\lambda) + D(\lambda)) \left(\frac{\lambda}{5500 \text{ \AA}} \right)^n, \quad (2)$$

where $k(\lambda)$ is Calzetti et al. (2000) attenuation curve and $D(\lambda)$ is the Lorentzian-like Drude profile parameterizing the UV bump. We use the $D(\lambda)$ definition by Kriek & Conroy (2013). This attenuation model has three parameters; $\hat{\tau}_{\text{dust},2}$, the ratio of $\hat{\tau}_{\text{dust},1}$ to $\hat{\tau}_{\text{dust},2}$, and the index n . We set all three parameters as free parameters and assume their priors to be uniform between 0 and 4 for $\hat{\tau}_{\text{dust},2}$, uniform between 1.0 and 0.4 for n , and a normal distribution with $\mu = 1.0$ and $\sigma = 0.3$ truncated at 0.0 and 2.0 for $\hat{\tau}_{\text{dust},1}/\hat{\tau}_{\text{dust},2}$.

SFH: We fix the number of age bins for non-parametric SFH fitting to eight and calculate the SFR for each bin. Leja et al. (2019) have examined the dependence of the number of age bins on the reconstructed results and found that there is no significant dependence if the number of age bins is greater than 4 . We also fix the recent five age bins to $[0 \text{ yr}, 10^{7.5} \text{ yr}]$, $[10^{7.5} \text{ yr}, 10^8 \text{ yr}]$, $[10^8 \text{ yr}, 10^{8.33} \text{ yr}]$, $[10^{8.33} \text{ yr}, 10^{8.67} \text{ yr}]$, and $[10^{8.67} \text{ yr}, 10^9 \text{ yr}]$ in lookback time t_i , and set the remaining three age bins by splitting equally $\log t_i$ in the logarithmic interval from 10^9 yr to $0.95t_H$.

The typical priors of non-parametric SFHs used in PROSPECTOR are the continuity prior (Leja et al. 2019; Johnson et al. 2021) and the Dirichlet prior (Leja et al. 2017; Leja et al. 2019). The continuity prior is for the ratio of SFRs in adjacent age bins, and the Student's-t distribution is widely used. For the Dirichlet prior, we assume a Dirichlet distribution (Leja et al. 2017; Leja et al. 2018) for the fractional sSFR in each age bin. Leja et al. (2019) have examined the prior dependence of SFHs by applying PROSPECTOR on mock data, finding that both priors can reconstruct the shape of the assumed SFH in mock data. However, they have also found that the continuity and Dirichlet priors tend to reconstruct the SFH “dispersively” and “concentratedly”, respectively. In this study, we use both priors and compare the results. We

have eight age bins, and total stellar mass is also a free parameter. Thus, the number of free parameters for the SFH is seven for both priors: seven SFR ratios between the adjacent bins for the continuity prior and seven Dirichlet parameters.

Spectrophotometric calibration: MaNGA data are already flux-calibrated by the DRP. However, for any galaxy, the area of IFU spectroscopy is different from photometric apertures. We apply the spectrophotometric calibration model in PROSPECTOR to do aperture correction. This model fits a polynomial calibration function to scale the input observed spectrum to model spectra so that its pseudo photometry is consistent with the observed multi-band photometry (Johnson et al. 2021 for detail). We confirm that this calibration model works well with mock data fitting results.

Emission-line marginalization: Because PROSPECTOR assumes all nebular emission lines to originate from star formation, our SED fitting will fail to reconstruct the spectrum around an observed emission line if the line is contaminated by a LIER, an AGN, or shock heating. To avoid this problem, we marginalize the amplitude of each emission line in each fitting step. We fit for the velocity dispersion of gas, σ_{gas} , assuming a uniform prior between 10 km/s and 300 km/s. We also confirm that introducing line marginalization can improve the model spectrum around a complex single-line feature consisting of narrow emission and broad absorption lines.

Likelihood calculation and the outlier model:

Finally, we calculate the likelihood \mathcal{L} as the product of the likelihood for the photometric data $\mathcal{L}_{\text{phot}}$ and the spectrum $\mathcal{L}_{\text{spec}}$, as

$$\ln \mathcal{L} = \ln \mathcal{L}_{\text{phot}} + (1 - f_{\text{out}}) \ln \mathcal{L}_{\text{spec}} + f_{\text{out}} \ln \mathcal{L}_{\text{out}}, \quad (3)$$

where \mathcal{L}_{out} is the penalty from the outlier model described below (equation 5). Here, \mathcal{L} is calculated on the assumption of Gaussian uncertainties, as

$$\ln \mathcal{L}(f, m, \sigma) = - \sum_i^N \frac{(f_i - m_i)^2}{2\sigma_i^2}, \quad (4)$$

where f , σ , and m are the observed flux density, its uncertainty, and the model flux density, respectively.

We apply the outlier model (Hogg et al. 2010; Johnson et al. 2021) to ignore outlier data not fitted well by the model spectrum (e.g., cosmic rays, airglow lines, and complex line features). On the assumption that a certain percentage f_{out} of data points are outliers, this model adds a penalty term in the likelihood calculation. The penalty term is calculated by multiplying the uncertainty by s_{out} for all data points, as

$$\ln \mathcal{L}_{\text{out}}(f, m, \sigma) = - \sum_i^N \frac{(f_i - m_i)^2}{2(s_{\text{out}}\sigma_i)^2}. \quad (5)$$

With this penalty term, the model becomes less sensitive to the spectral data. In this study, we applied $s_{\text{out}} = 50$.

Table 1 summarizes the free parameters and their priors. This parameter setting is determined by referring to the run time, the distribution of each parameter obtained from several test runs, the range of each parameter in the Pipe3D and the MaNGA targeting catalog, and settings in some previous studies with PROSPECTOR (Tacchella et al. 2022).

As an example, figure 3 shows the observed and modeled (best-fit) spectra and photometry of a galaxy at $z = 0.044$ (plateifu:10216-6102). We calculate χ^2 values for spectroscopic data (χ_{spec}^2) and photometric data (χ_{photo}^2) separately. We find that the median of χ^2/N_{data} (N_{data} is the number of data points) for the whole sample is $\chi_{\text{spec}}^2/N_{\text{data,spec}} = 1.15_{-0.62}^{+1.82}$ and $\chi_{\text{photo}}^2/N_{\text{data,photo}} = 2.44_{-1.51}^{+3.85}$. While the median $\chi_{\text{spec}}^2/N_{\text{data,spec}}$ value is reasonable ($\simeq 1$), we find that objects whose spectra around the short-wavelength end are of poor quality have large $\chi_{\text{spec}}^2/N_{\text{data,spec}}$. Indeed, the $\chi_{\text{spec}}^2/N_{\text{data,spec}}$ of those objects decreases close to unity if the data around the short-wavelength end are excluded. On the other hand, the large median $\chi_{\text{photo}}^2/N_{\text{data,photo}}$ value is primarily because the WISE data (especially W4) of most objects are not reproduced well. This problem may be resolved by adding new free parameters to the dust model.

The joint posterior distribution plot (corner plot) of six key parameters for the same example galaxy as figure 3 is shown in figure 4. This galaxy is one of the rejuvenation galaxies selected with the method described in section 3.2. We find that basic parameters such as M^* , Z^* and $\hat{\tau}_{\text{dust},2}$ are strongly constrained. The estimated SFH distribution shows that this galaxy experienced rejuvenation at $t_l = 10^8$ yr with $\text{SFR}_{32 \text{ Myr}} \sim 10M_{\odot}/\text{yr}^{-1}$, and the resumed star formation ended in the most recent time bin. As the strong negative correlation between $\hat{\tau}_{\text{dust},2}$ and $\log(Z^*/Z_{\odot})$ suggests, dust-metallicity degeneracy can also be seen in our results. However, the 1σ range of $\hat{\tau}_{\text{dust},2}$ and $\log(Z^*/Z_{\odot})$ is much smaller than the median value of each parameter, suggesting that our method can constrain these parameters reasonably well. Besides, $\hat{\tau}_{\text{dust},2}$ and $\log(Z^*/Z_{\odot})$ are not strongly correlated with the SFRs in the recent three bins that are very sensitive to the selection of RGs (see section 3.2 for our selection method). These results support our RG selection method.

We also check whether PROSPECTOR can select true RGs under this setting by running it on mock data (section 4) and comparing the results for the real data with existing catalogs (appendix).

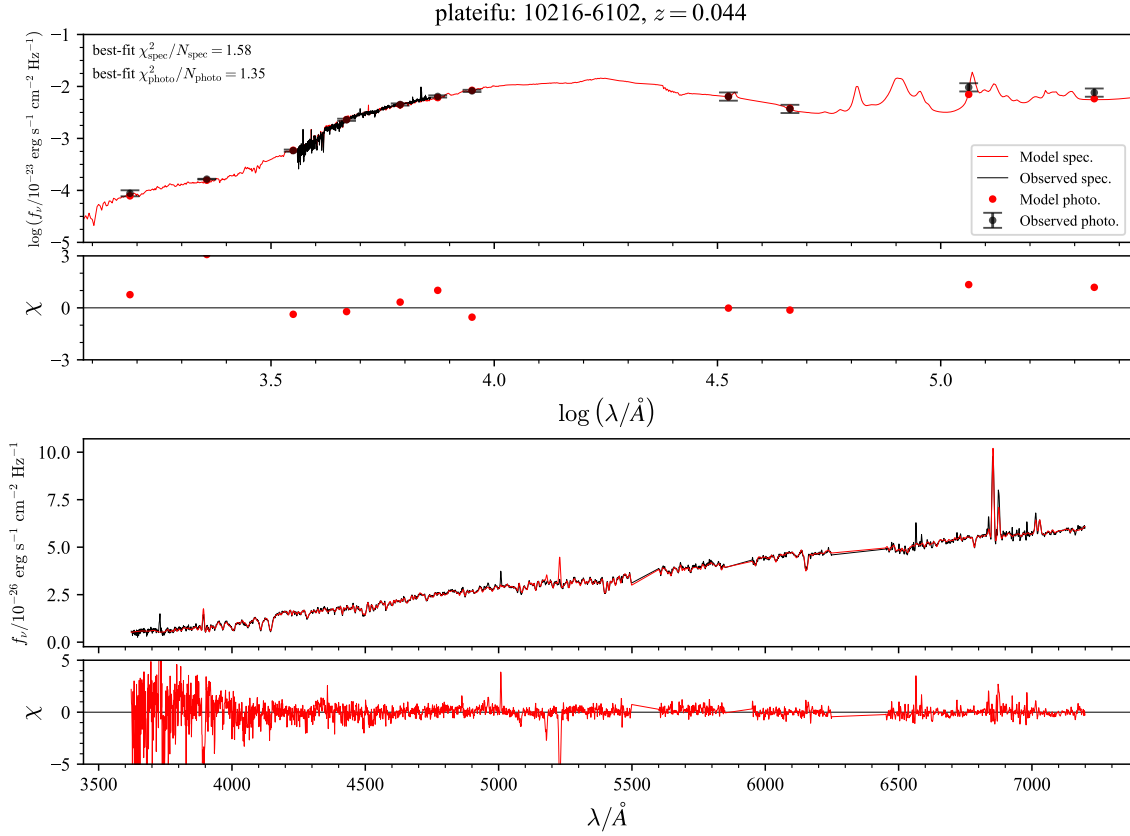


Fig. 3. The top (bottom) panel compares photometric (spectroscopic) data with the best-fit model for a galaxy at $z = 0.044$ (plateifu:10216-6102), with the lower plot in each panel showing $\chi = (f_{\nu,\text{obs}} - f_{\nu,\text{model}}) / \sigma$.

Table 1. Free parameters and their priors for PROSPECTOR fitting

parameter	Description	prior
$\log(M^*/M_\odot)$	total stellar mass	Uniform: min=8, max=13
$\log(Z^*/Z_\odot)$	stellar metallicity	Uniform: min=-2, max=0.19
$\log U$	ionization parameter	Uniform: min=-4, max=-1
n	power-law index of the dust attenuation curve of the diffuse dust	Uniform: min=-1, max=0.4
$\hat{\tau}_{\text{dust},2}$	optical depth of the diffuse dust attenuation	Uniform: min=0, max=4
$\hat{\tau}_{\text{dust},1}$	optical depth of the birth-cloud dust attenuation	Clipped normal in $\hat{\tau}_{\text{dust},1} / \hat{\tau}_{\text{dust},2}$: min=0, max=2, $\mu = 1$, $\sigma = 0.3$
σ_*	velocity dispersion of the stellar component	Uniform: min=10 km/s, max=300 km/s
σ_{gas}	velocity dispersion of gas	Uniform: min=10 km/s, max=300 km/s
f_{out}	outlier fraction of spectral data points	Uniform: min= 10^{-5} , max=0.5
SFR ratios	$\Delta \log \text{SFR}$ between adjacent age bins (only when using the continuity prior)	Student's-t distribution with $\sigma = 0.3$ and $\nu = 2$
Dirichlet parameters	weight of SFRs in each age bin (only when using the Dirichlet prior)	Dirichlet distribution with $\alpha_D = 1$

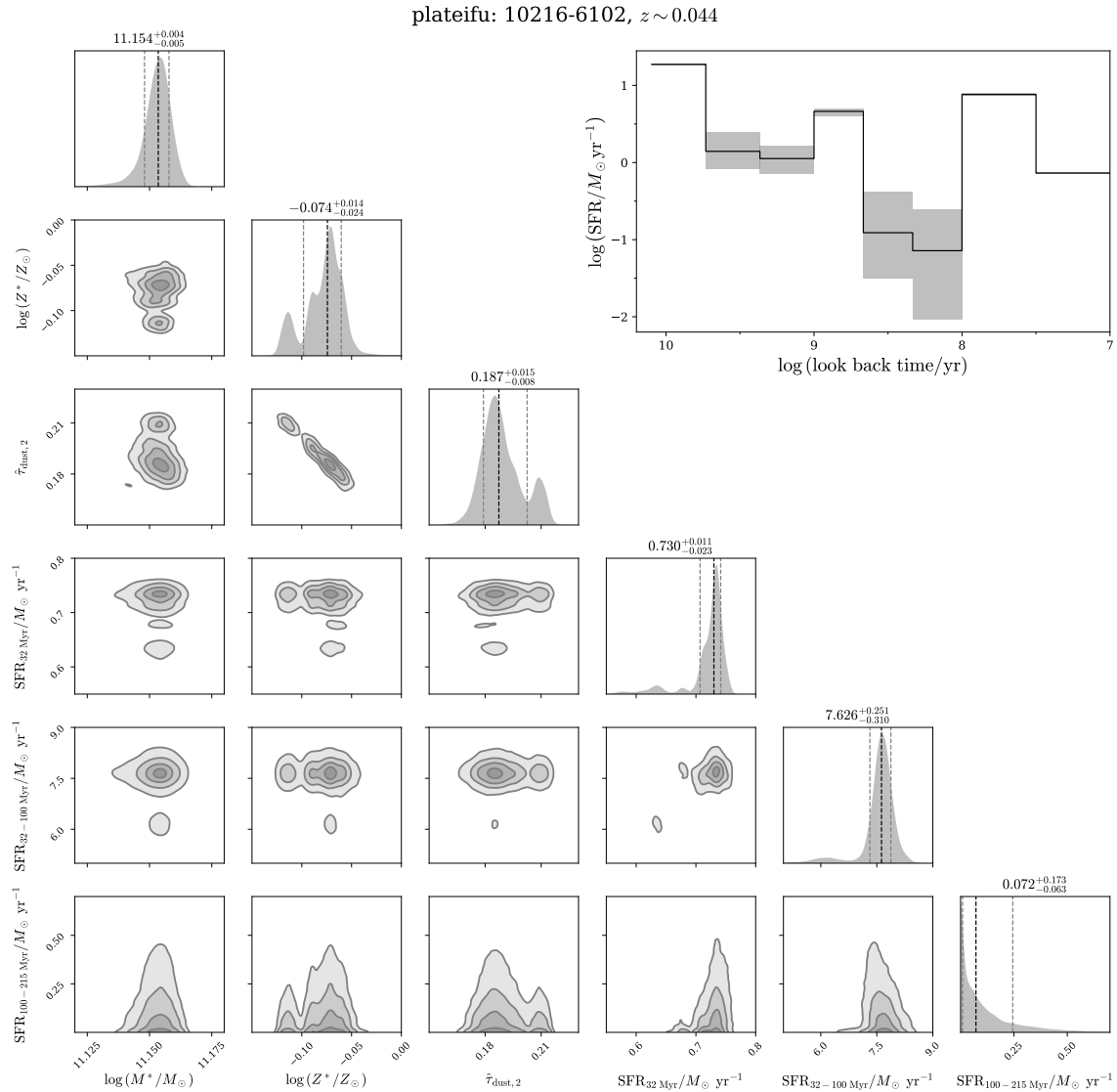


Fig. 4. Joint posterior distribution plot (corner plot) of M^* , Z^* , $\hat{\tau}_{\text{dust},2}$, and SFRs in the recent three age bins ($[0 \text{ yr}, 10^{7.5} \text{ yr}]$, $[10^{7.5} \text{ yr}, 10^8 \text{ yr}]$, and $[10^8 \text{ yr}, 10^{8.33} \text{ yr}]$) for the example galaxy in figure 3 (plateifu:10216-6102, $z = 0.044$). The diagonal panels show the posterior distribution of each parameter with black and gray dashed lines indicating the median and the 1σ confidence level, and the panels below each diagonal panel show correlations with the remaining parameters. The upper right panel shows the estimated SFH of this galaxy; the solid black line indicates the median SFR, with a gray shaded region corresponding to the 1σ confidence level of the fit.

3.2 Selection method

As introduced in section 1, RGs are galaxies that have restarted star formation after being quenched. We select RGs using reconstructed SFHs.

For each galaxy, first, we calculate $\mathcal{D}(z)$, the fraction of the mass that will be formed by the given redshift z if the star formation rate is constant with $\text{SFR}(z)$, as

$$\begin{aligned} \mathcal{D}(z) &= \text{sSFR}(z) \times t_H(z) \\ &= \frac{\text{SFR}(z)}{M^*(z)} \times t_H(z), \end{aligned} \quad (6)$$

where $t_H(z)$ is the age of the universe at z . Then, we classify the galaxy in each age bin into an SFG, GV, or QG using $\mathcal{D}(z)$ to track the evolution of type with cosmic time. We determine the threshold \mathcal{D} for classification by fitting the $\log \mathcal{D}$ distribution with a three-component mixture Gaussian profile. Figure 5 shows the fitting result of the $\log \mathcal{D}$ distribution in the latest age-bin, i.e., the bin from $t = 10^{7.5}$ yr to the observed time for the continuum prior. We have also confirmed that the Dirichlet prior gives almost the same results. We fix the SFG/GV and GV/QG boundaries at $\log \mathcal{D} = -1.2$ and -1.8 , respectively, based on the 1σ values of the peaks corresponding to SFGs and QGs.

Because the location of the SFMS depends on z (e.g., Noeske et al. 2007; Elbaz et al. 2007; Whitaker et al. 2012; Speagle et al. 2014; Renzini et al. 2015; Tomczak et al. 2016; Pearson et al. 2018; Popesso et al. 2023), the threshold \mathcal{D} value can vary with redshift. For example, Tacchella et al. (2022) have used 1/3 and 1/20 for the \mathcal{D} thresholds (-0.48 and -1.3 for $\log \mathcal{D}$ thresholds) with a $z \sim 0.8$ sample. However, because our RG selection only focuses on the most recent 10^8 years much shorter than the timescale of the change of the SFMS location, we can ignore the redshift dependence of the \mathcal{D} threshold value in this study.

Finally, we define an RG as a galaxy that returned to a GV or SFG from a QG within the recent 1×10^8 yr. This means t_{rej} , the lookback time when a rejuvenation started, is either 10^8 yr or $10^{7.5}$ yr in this study. In other words, we define an RG as follows,

- $t_{\text{rej}} = 10^{7.5}$ yr
 $[0, 10^{7.5}$ yr]: GV or SFG
 $[10^{7.5}$ yr, $10^{8.0}$ yr]: QG
- $t_{\text{rej}} = 10^{8.0}$ yr
 $[0, 10^{7.5}$ yr]: QG, GV or SFG
 $[10^{7.5}$ yr, $10^{8.0}$ yr]: GV or SFG
 $[10^{8.0}$ yr, $10^{8.33}$ yr]: QG

It is conceivable that galaxies restart star formation before 10^8 yr. However, the age-bin setting in our PROSPECTOR run is equally spaced in logarithmic space; thus, return-

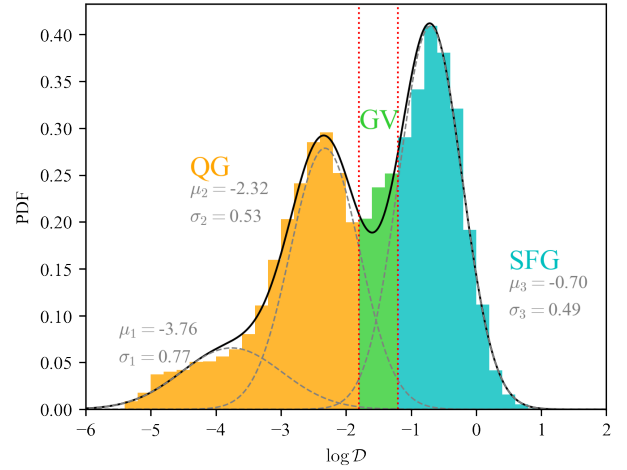


Fig. 5. The colored histogram is the distribution of \mathcal{D} values in the most recent age-bin obtained with the continuity prior. The solid black line indicates the result of mixture Gaussian fitting to the histogram, with three gray dashed lines being the three Gaussian components. The best-fit values of each Gaussian are written in gray. Red dotted lines indicate the threshold \mathcal{D} values and the histogram is colored according to the classification (orange, green, and cyan for QGs, GVs, and SFGs).

ing to a GV or SFG in an age-bin older than 10^8 yr is a different-timescale event from the above definition. For this reason, we limit t_{rej} to $10^{7.5}$ and $10^{8.0}$ and focus on the rejuvenation in the recent ~ 100 Myr.

We apply the above selection method to chain data obtained from PROSPECTOR runs and calculate p_{RG} , the probability that the galaxy is an RG, as

$$p_{\text{RG}} = \frac{n_{\text{chain, RG}}}{n_{\text{chain}}}, \quad (7)$$

where n_{chain} is the length of all chains and $n_{\text{chain, RG}}$ is the number of chains classified as an RG. As mentioned above, our RG definition has two patterns in terms of t_{rej} , and we calculate p_{RG} as the total RG probability; as the sum of the probability of each t_{rej} pattern to select galaxies more likely to have rejuvenated regardless of their t_{rej} . We define the t_{rej} of a given galaxy as the timing with a higher p_{RG} .

Each galaxy has two p_{RG} values: one with the continuum prior, $p_{\text{RG, con}}$, and the other with the Dirichlet prior, $p_{\text{RG, Dir}}$. We select galaxies with $p_{\text{RG, con}} > 0.8$ and $p_{\text{RG, Dir}} > 0.5$ as RGs. We determine these criteria with the SED fitting results of our parent sample and the mock data as described in sections 4.3.

Figure 6 shows examples of the specific star-formation history (sSFH) for the selected RGs. Note that our method depends on the classification into QG/GV/SFG and hence that a galaxy with a clearly increasing sSFR may have a relatively low p_{RG} because its sSFR before rejuvenation is just below the threshold between QGs and GVs (e.g., 8078-6104 in figure 6 column 5 row 3).

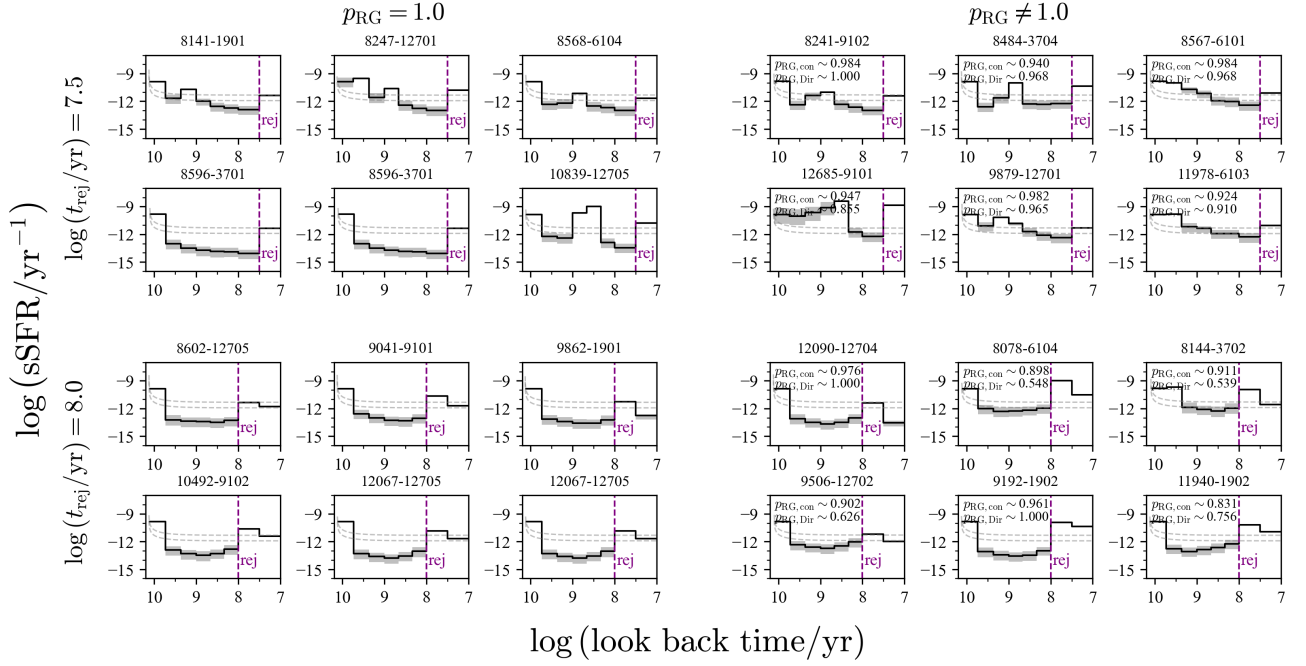


Fig. 6. Examples of the sSFHs of selected high- p_{RG} RGs with $p_{\text{RG}} = 1$ (rows 1, 2, and 3) and $p_{\text{RG}} \neq 1$ (rows 4, 5, and 6, where p_{RG} is given in each panel). Lines 1 and 2 are for objects with $\log(t_{\text{rej}}/\text{Myr}) = 7.5$ while lines 3 and 4 for $\log(t_{\text{rej}}/\text{Myr}) = 8$, where t_{rej} is indicated by a purple dashed line. In each panel, the solid black line indicates the median sSFR, with a gray shaded region corresponding to the 1σ confidence level of the fit. The gray dashed lines in each panel show the SFG/GV/QG thresholds.

4 Verification of our RG selection Method

We run PROSPECTOR with mock data to verify that our method works well. Since SED fitting with a non-parametric SFH has been pointed out to have prior dependence (Leja et al. 2019), we also discuss prior dependence.

4.1 Making mock data

We make mock data at $z = 0.1$ with PROSPECTOR. Since we also use PROSPECTOR in the SED fitting (see section 3.1 for the fitting process), we cannot evaluate the validity of the model spectra in this validation. The purpose of using a mock sample is only to discuss whether our fitting process can reconstruct the correct SFH and select RGs even with noise.

We construct two mock samples, a single-peak-SFH sample and a double-peak-SFH sample, based on the delayed-tau SFH, one of the popular parametric SFHs.

Double-peak-SFH mock sample: To examine if our selection method can select RGs and distinguish RGs from non-rejuvenation galaxies (nRGs) with RG-like SFHs, we make mock data with double-peak SFHs that are a superposition of two delayed-tau models as follows,

$$\text{SFH}(t) = C_1 (t_1 - t_l) \exp\left(-\frac{t_1 - t_l}{\tau_1}\right) + \begin{cases} C_2 (t_2 - t_l) \exp\left(-\frac{t_2 - t_l}{\tau_2}\right) & (t_l > t_1) \\ 0 & (t_l > t_2), \end{cases} \quad (8)$$

where τ_1 (τ_2) is the time scale of the first (second) delayed tau model, t_1 (t_2 [$< t_1$]) is the lookback time when the first (second) delayed tau star formation starts, and C_1 (C_2) is a coefficient of the first (second) delayed tau model. We calculate C_1 and C_2 from f , the ratio of the formed mass in the second delayed tau SFH to the total M^* . We fix t_1 as $0.95t_H$, and M^* as $10^{11} M_\odot$. In equation (8), the first term shows the typical galaxy evolution scenario of quenching after active star formation. The second term corresponds to a rejuvenation or pseudo-rejuvenation event. Note that the first term has a negative value in $t_l > t_1$; thus, we calculate the SFH only for $t_l > t_1$.

To examine various RGs and pseudo RGs, we generate 144 SFHs as a combination of the following parameters,

- f : 10^{-1} , 10^{-2} , 10^{-3} , 10^{-4}
- τ_1 : 1 Gyr, 1.5 Gyr, 2 Gyr
- $(t_H - t_2)/\tau_2$: 1, 10, 50
- $t_H - t_2$: 10^7 yr, $10^{7.5}$ yr, 10^8 yr, $10^{8.5}$ yr.

The specific star-formation histories (sSFHs) of the mock data are shown in figure 7. Note that although these mock galaxies have two star-formation peaks, not all mock galaxies are RGs. For example, if we apply our definition

introduced in section 3.2, some galaxies were SFGs or GVs just before the start of the second star formation, and these are not classified as RGs. Besides, we should also note that some galaxies with $f \sim 0.1$ have extremely high SFRs such as $\log(\text{SFR}/M_\odot \text{ yr}^{-1}) \gtrsim 3$.

We calculate mock SEDs with the above modeled SFHs. We add dust and nebular emissions to the stellar continuum. We fix $\log(Z/Z_\odot)$ at -0.5 and $\hat{\tau}_2$ at 0.3 , which are similar to the estimated values for our galaxy sample as shown in appendix. We assume a Chabrier (2003) initial mass function as in the case of real data. Then, we use the mock SEDs to calculate mock photometric and spectral data by adding noise following the S/N values shown in the table 2. These S/N are mainly based on the median S/N for the main sample, but we fix the mock S/N to 20 for $S/N > 20$ and 5 for $S/N > 5$ WISE photometry to account for possible systematic errors, such as aperture correction errors. Thus, our mock data are more conservative than the real data in terms of S/N .

Single-peak-SFH mock sample: To discuss the possibility that galaxies without rejuvenation or a second star-formation event are erroneously selected, we also generate mock data with single peak SFHs using the single delayed-tau model as,

$$\text{SFH}(t) = C_1 (t_1 - t_l) \exp\left(-\frac{t_1 - t_l}{\tau_1}\right). \quad (9)$$

This time, we also change t_1 : the lookback time of starting star formation. We generate 25 SFHs as a combination of the following parameters,

- τ_1 : 2.00×10^8 yr, 3.56×10^8 yr, 6.32×10^8 yr, 1.12×10^9 yr, 2.00×10^9 yr
- $t_H - t_1$: 1.25×10^9 yr, 2.19×10^9 yr, 3.84×10^9 yr, 6.74×10^9 yr, 1.18×10^{10} yr,

where τ_1 is equally sampled in log space between 2×10^8 yr and 2×10^9 yr, and $t_1 - t_l$ is equally sampled in log space between $0.1t_H$ and $0.95t_H$.

The sSFHs of the single-peak-SFH mock sample are shown in figure 8. They have a wide range of current sSFRs over the SFR, GV, and QG regimes and have never experienced a second active star formation, including rejuvenation.

In the calculation of mock SEDs, we make the same assumptions for the metallicity, dust extinction, and IMF as for the double-peak-SFH mock sample.

4.2 Basic parameters

Using the settings described in section 3.1, we run PROSPECTOR on the mock galaxies and estimate their SFH and other parameters.

We compare the estimated parameters with the as-

sumed ones in the mock data in figure 9. Figures 9 (a), (b), and (c) shows the distribution of M^* , Z , and $\hat{\tau}_{2,\text{dust}}$, respectively. We find that PROSPECTOR reproduces the values of these parameters well. We also find that there are no large differences between the results for the two priors.

Next, we test how well the assumed SFHs are reconstructed by calculating mean SFRs in three bins: $t_l < 100$ Myr, $100 \text{ Myr} < t_l < 1000$ Myr, and $t_l > 1000$ Myr (figure 9 (d), (e), and (f), respectively). Figure 9 (d) compares $\text{SFR}_{100 \text{ Myr}}$, the SFR in $t_l < 100$ Myr, showing a strong correlation between the mock and estimated values. For galaxies with low assumed SFRs ($\log \text{SFR}_{100 \text{ Myr}} \lesssim -0.5$), the continuity prior reproduces the mock values better than the Dirichlet prior. However, both priors overestimate the SFRs by about 0.3-0.4 dex.

Figure 9 (e) compares $\text{SFR}_{100-1000 \text{ Myr}}$, the SFR in $100 \text{ Myr} < t_l < 1000$ Myr, finding a similarly strong correlation. For galaxies with medium assumed SFRs ($\log \text{SFR}_{100-1000 \text{ Myr}} \sim 0$), the continuity prior often underestimates $\text{SFR}_{100-1000 \text{ Myr}}$. On the other hand, for galaxies with low assumed SFRs ($\log \text{SFR}_{100-1000 \text{ Myr}} \sim -2$), the Dirichlet prior often overestimates $\text{SFR}_{100-1000 \text{ Myr}}$.

Figure 9 (f) compares $\text{SFR}_{\text{before } 1000 \text{ Myr}}$, the SFR in $t_l > 1000$ Myr, and finds a weak correlation in both priors. This study does not focus on past star formations. However, because we define RGs with sSFHs, underestimation of the old stellar population may cause an overestimation of the current sSFR and affect our selection. We discuss this problem in section 4.3.

The distribution of estimated metallicities (figure 9 (b)) shows a small peak with lower metallicities ($\log(Z^*/Z_\odot) \lesssim -0.8$) in addition to the primary peak around the assumed value ($\log(Z^*/Z_\odot) \sim -0.5$). The galaxies around the small peak have underestimated masses ($\log(M^*/M_\odot) \lesssim 10.7$). The double-peak-SFH mock sample have 16 galaxies with $\log(Z^*/Z_\odot) < -0.8$, and 15 of them ($\sim 94\%$) have $t_H - t_2 = 10^7$ yr. Besides, ten and six (about 63 and 38%) have $f = 0.1$ and 0.01 , respectively. The $\text{SFR}_{\text{before } 1000 \text{ Myr}}$ of these galaxies are greatly underestimated. It is likely that PROSPECTOR cannot reconstruct old star formation due to an extremely large contribution from recent star formation, i.e., the young stellar population. Thus, PROSPECTOR may underestimate the stellar mass and metallicity of galaxies with very recent and active resumed star formation. However, since many $f = 0.1$ SFHs have extremely high SFRs over $10^3 M_\odot \text{ yr}^{-1}$ for low- z galaxies, this underestimation is not a serious problem in applying to real data. However, this underestimation may need to be considered to search for RGs in the high- z universe because they have low stellar masses and high SFRs.

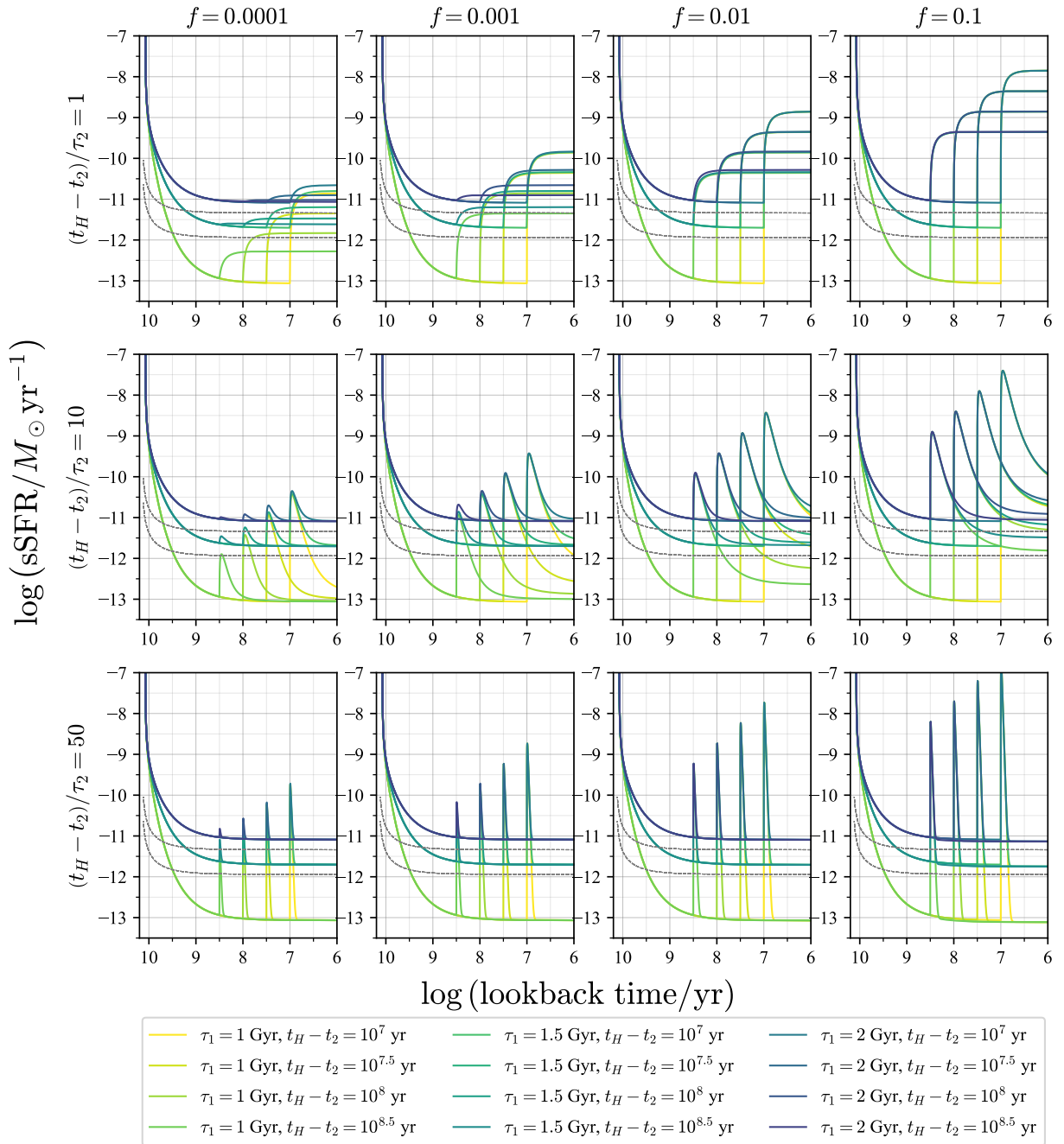


Fig. 7. The sSFHs of the double-peak-SFH mock sample. Rows 1, 2, 3, and 4 are for $f = 0.0001, 0.001, 0.01,$ and $0.1,$ respectively, while lines 1, 2, and 3 are for $(t_H - t_2)/\tau_2 = 1, 10,$ and $50,$ respectively. Different colors of lines correspond to different combinations of τ_1 and $t_H - t_2$. Gray dashed lines show the boundaries of SFG/GV/QG classification.

Table 2. Median S/N for the main sample and the assumed S/N in making mock observation data.

	GALEX		SDSS				WISE				MaNGA		
	FUV	NUV	u	g	r	i	z	W1	W2	W3	W4	blue	red
Median	5.1	17.6	42.9	290.1	357.6	341.3	167.6	485.7	155.7	17.8	4.5	23.0	46.6
Mock	5.1	17.6	20	20	20	20	20	5	5	5	4.5	20	20

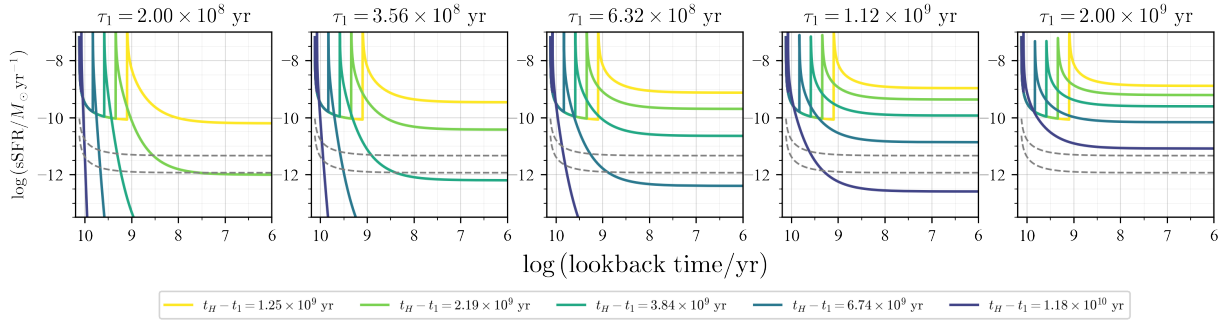


Fig. 8. The sSFHs of the single-peak-SFH mock sample with $\tau_1 = 2.00 \times 10^8$ yr, 3.56×10^8 yr, 6.32×10^8 yr, 1.12×10^9 yr, and 2.00×10^9 yr from left to right. Different colors of lines indicate different $t_H - t_1$. Gray dashed lines show the boundaries of SFG/GV/QG classification.

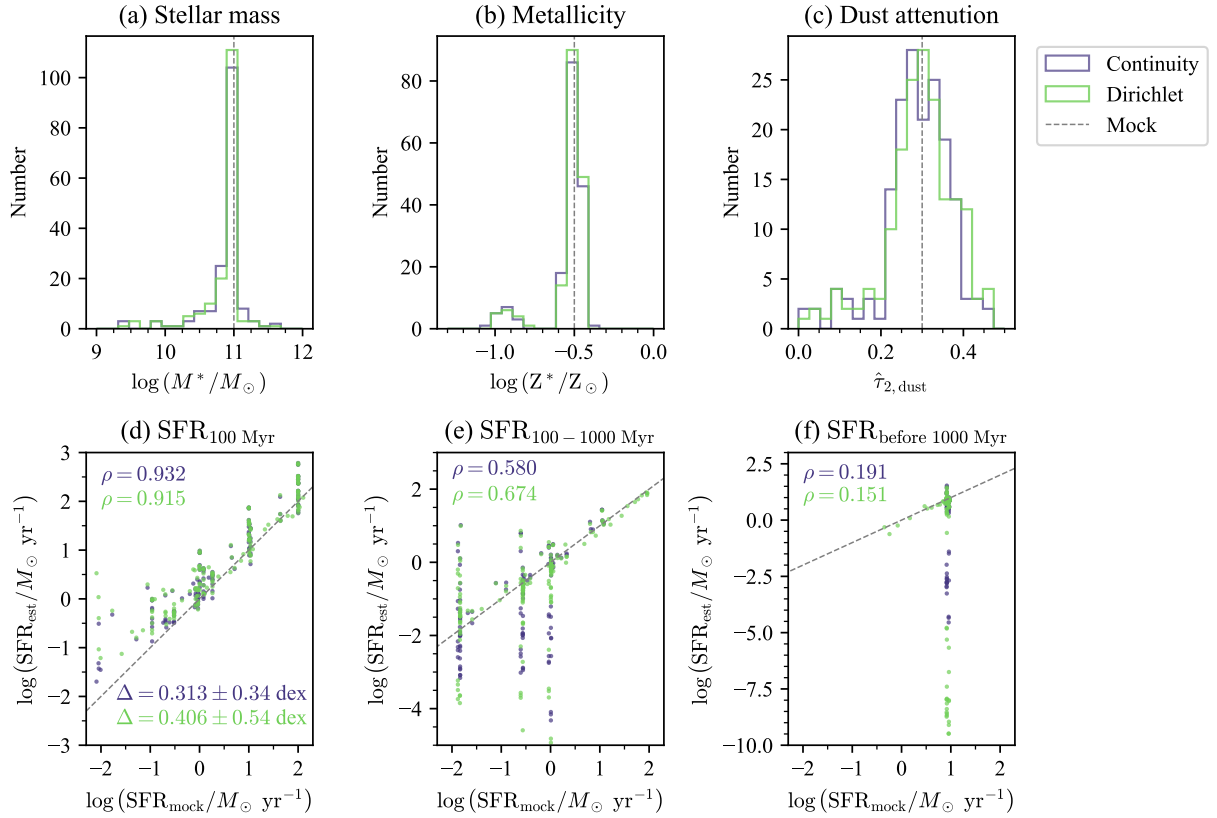


Fig. 9. Panels (a), (b), and (c) show the histograms of estimated total stellar masses, metallicities, and optical depths of the diffuse dust attenuation, respectively, for the continuity prior in purple and the Dirichlet prior in green. The assumed values (the true answers) are indicated by gray dashed lines. Panels (d), (e), and (f) compare estimated SFRs with mock SFRs within 100 Myr, between 100 Myr and 1000 Myr, and before 1000 Myr, respectively, for the continuity prior in purple and the Dirichlet prior in green. Spearman's correlation coefficient ρ for each prior is shown in the upper left corner of each panel. The solid black lines show the $y = x$ relation. We perform fitting with $y = x + \Delta$ only for panel (d). Generally, Our method reconstructs each parameter well, except for SFR in old age ($\text{SFR}_{\text{before 1000 Myr}}$).

To evaluate how well PROSPECTOR can detect rejuvenation events, we calculate μ , the ratio of the formed mass in the recent 100 Myr to the total stellar mass. Note that μ is different from f because we calculate μ by dividing the formed mass in the recent 100 Myr by the total M^* , while calculating f by dividing the formed mass in the second delayed-tau model by the total M^* . Although estimating f from reconstructed SFHs is challenging, μ can be easily calculated. Figure 10 compares estimated μ with assumed ones. We find that PROSPECTOR tends to overestimate μ about 0.5 dex. This tendency is mainly due to the overestimation of $\text{SFR}_{100 \text{ Myr}}$ (about 0.4 dex higher).

4.3 RG selection

The correlation between $p_{\text{RG,con}}$ and $p_{\text{RG,Dir}}$ for mock and real galaxies is shown in figure 11 (a). We classify mock galaxies into RGs and nRGs in the same manner as for real galaxies using reconstructed SFHs. These mock RGs and nRGs are shown in purple and orange, respectively, in figure 11 (a). We find that almost all the mock RGs have $p_{\text{RG,con}} > p_{\text{RG,Dir}}$.

For real galaxies, a high Spearman's correlation coefficient of $\rho \simeq 0.79$ is obtained. However, the value drops to $\rho \simeq 0.38$ if limited to sources with intermediate p_{RG} ($0.1 < p_{\text{RG,con}} < 0.9$), suggesting that the high coefficient value for all galaxies is caused by very RG-like ($0.9 < p_{\text{RG}}$) and very non-RG-like ($p_{\text{RG}} < 0.1$) galaxies. We note that both priors are relatively consistent with each other in that they can correctly select both very RG-like and very non-RG-like objects.

Despite the high correlation coefficient, real galaxies (and mock galaxies) are not evenly distributed around the equality line; objects with medium $p_{\text{RG,con}}$ values tend to be lower than the line. This distribution may be explained as follows. As seen in section 4.2, the continuity prior tends to give lower $\text{SFR}_{100-1000 \text{ Myr}}$ and higher $\text{SFR}_{\text{before } 100 \text{ Myr}}$ than the Dirichlet prior, especially for low SFR objects. This means that the continuity prior tends to reconstruct more V-shaped, or more RG-like, SFHs than the Dirichlet prior. Thus, $p_{\text{RG,con}}$ is likely to be higher than $p_{\text{RG,Dir}}$ especially for low to medium $p_{\text{RG,con}}$ objects, which are often located around the boundary of QGs and GVs.

Considering these trends in the mock and main parent samples, we set up three regions (A), (B), and (C) in the $p_{\text{RG,Dir}} - p_{\text{RG,con}}$ plane as candidate regions for RG selection and discuss which region selects RGs best. Regions (A), (B), and (C) are defined as,

- (A) : $p_{\text{RG,Dir}} > 0.5$ and $p_{\text{RG,con}} > 0.8$,
- (B) : $p_{\text{RG,Dir}} < 0.4$ and $p_{\text{RG,con}} > 0.6$,
- (C) : $p_{\text{RG,Dir}} < 0.2$ and $p_{\text{RG,con}} < 0.2$.

The SFHs and sSFHs of mock RGs and mock nRGs in each region are shown in figure 11 (b). The parameters of the single-peak-SFH mock sample in each region are also shown in table 3.

In region (A), we have 12 mock galaxies, and six of them are classified as RGs with mock SFHs. All six RGs have $f = 0.001$ and $t_H - t_2 = 10^7 \text{ yr}, 10^{7.5} \text{ yr}$. Similarly, all the mock nRGs in region (A) also have $f = 0.001$ and $t_H - t_2 = 10^7 \text{ yr}$. From these results, galaxies in region (A) are likely to have experienced a very recent second SF with $f \sim 0.001$.

Then, in region (B), we have 18 mock galaxies, and five of them are classified as RGs with mock SFHs. As far as we can judge from the mock data, the contamination rate in region (B) is 72%, which is higher than in region (A) (50%). Region (B) has more mock galaxies with $f = 0.01$ and $t_H - t_2 = 10^{7.5} \text{ yr}$ than region (A).

Finally, in region (C), we have 106 mock galaxies, and 21 of them are classified as RGs with mock SFHs. The contamination rate is 80%, the highest in the three regions. Most single-peaked-SFH mock galaxies (22/25) are distributed in region (C), meaning that our method can correctly diagnose single-peaked-SFH galaxies as nRGs. We find that mock RGs with $f = 0.0001, 0.01$, and 0.1 are concentrated in region (C) while there are no mock RGs with $f = 0.001$ there. Besides, most of the mock RGs with $t_H - t_2 \gtrsim 10^8 \text{ yr}$ are in region (C). Although our method focuses on rejuvenation within 10^8 yr , rejuvenation events starting from $t_i = 10^8 \text{ yr}$ may not be detected in our method.

Based on these results, we choose the region for RG selection. If we use region (A) to select RGs, the contamination rate of RG selection in mock data is 50% (6/12). However, the contaminants, i.e., nRGs in region (A), also have a recent second star formation with $f = 0.001$. Besides, region (A) does not include single-peaked-SFH mock galaxies. Therefore, region (A) can select RGs and RG-like secondary-star-formation galaxies with $f \sim 0.001$. Since the parameter distribution of mock galaxies should not be the same as the distribution of real galaxies, we cannot calculate the exact contamination rate. We can only affirm the possibility of selecting such contaminants.

Next, the completeness of RG selection using region (A) is found to be 17% (6/36). However, similar to the above discussion, we cannot know the exact completeness with our mock data. For example, as shown in figure 11(b), the mock SFHs in regions (B) or (C) have extremely high SFRs like $\text{SFR} \gtrsim 10^2 M_\odot \text{ yr}^{-1}$. In the low- z Universe, galaxies with such extremely high SFRs are extremely rare, and the settings of mock data may not be realistic. If we fo-

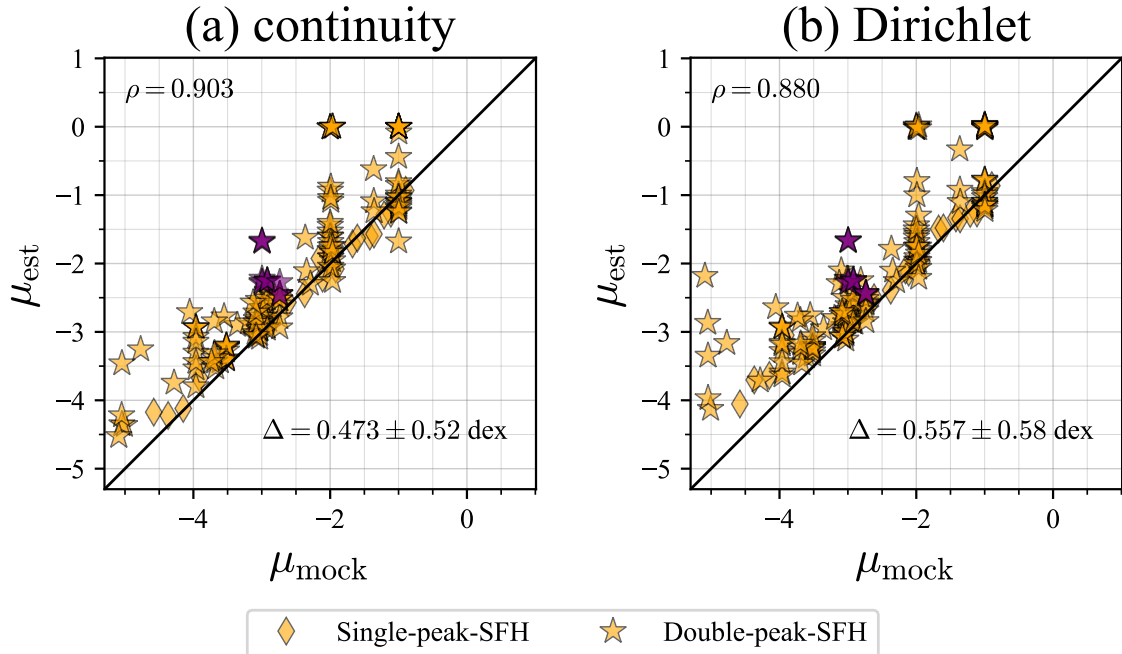


Fig. 10. Comparison of μ_{mock} calculated from mock SFHs with μ_{est} obtained from reconstructed SFHs with the continuity prior (panel [a]) and the Dirichlet prior (b). Diamonds are for single-peak SFH galaxies, and stars for double-peak-SFH galaxies. Yellow and purple colors mean nRGs and RGs, respectively. Spearman's correlation coefficient ρ is given in the upper left corner of each panel. The solid black lines show the $y = x$ relation. We perform fitting with $y = x + \Delta$, and the value of Δ and its 68% error is given in each panel. Our method can select only $\mu \sim 10^{-3}$ double-peak-SFH objects.

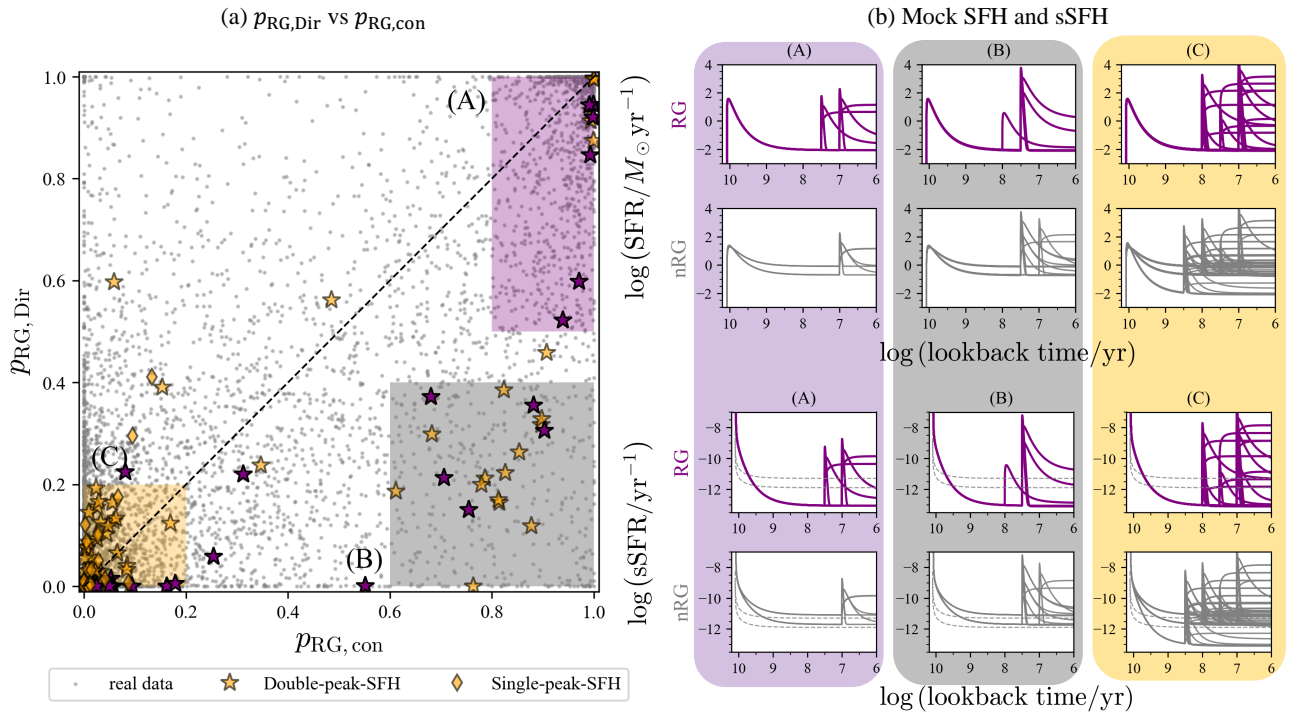


Fig. 11. (a) Comparison of $p_{\text{RG,con}}$ and $p_{\text{RG,Dir}}$. Diamonds, stars, and dots indicate single-peak-SFH mock galaxies, double-peak-SFH mock galaxies, and real data. Yellow and purple colors mean nRGs and RGs, respectively. The dashed black lines show the $y = x$ relation. Regions (A), (B), and (C) are shaded in purple, gray, and yellow, respectively. Region (A) can select $f = 0.001$ RGs with high completeness. (b) The mock SFHs and sSFHs of mock galaxies in each region. RGs and nRGs are separately plotted. In the sSFH plots, the gray dashed lines indicate the SFG/GV/QG boundaries.

cus only on galaxies with $f = 0.001$, the contamination is 67% (6/9). The results with mock data suggest that using region (A), we can detect weak rejuvenation events with high completeness, although maybe missing galaxies with strong rejuvenation. From these results, we decide to use region (A).

As for contamination, region (A) may select galaxies with a second star formation whose progenitors are not QGs but GVs or SFGs. As for completeness, region (A) can miss galaxies that have experienced strong rejuvenation with $f \gtrsim 0.01$ or weak rejuvenation with $f \sim 0.0001$. However, region (A) can select RGs with $f \sim 0.001$ with high completeness.

We use the results with the continuity prior in the remaining part of this paper. This is mainly because the continuity prior has a stronger correlation in $\text{SFR}_{100 \text{ Myr}}$ (figure 9 (d)) and in μ (figure 10). Besides, $p_{\text{RG,con}}$ tends to be higher for $f = 0.001$ mock RGs than $p_{\text{RG,Dir}}$, suggesting that the continuity prior is better in reproducing $f = 0.001$ rejuvenation events. Note that our selection method uses both $p_{\text{RG,con}}$ and $p_{\text{RG,Dir}}$ as introduced in section 3.2 and discussed above.

The low completeness of our selection method comes from difficulties in estimating non-parametric SFHs. For large- f galaxies ($f \gtrsim 0.01$), the light from the young stellar population overwhelms that from the old stellar population, i.e., the outshining problem (c.f., Maraston et al. 2010; Sorba & Sawicki 2018; Giménez-Arteaga et al. 2023; Narayanan et al. 2023). In contrast, for small- f galaxies ($f \sim 0.0001$), the light from the young stellar population is buried by that from the old stellar population. It will be important to reduce this uncertainty as much as possible by improving the method, e.g., improving the SED fitting technique and searching for indices to find RGs easily. The latter will become especially important in the future as data are increasing rapidly. Because the completeness of selecting $f = 0.001$ mock RGs is high, we focus on $f \sim 0.001$ RGs in this study. We will discuss the effects of this incompleteness in section 6.

Again, note that because the mock data are generated with PROSPECTOR, the comparison in this section cannot demonstrate the validity of model spectra. To further demonstrate the validity of our SED fitting results with PROSPECTOR, we also checked that the basic results, such as M^* and SFR, estimated with PROSPECTOR are strongly correlated with an existing SED fitting result, the Pipe3D DR17 catalog (Sánchez et al. 2022). The detail of this comparison is introduced in appendix.

Table 3. The number of mock galaxies with each mock parameter in each region.

	f					τ_1			$(t_H - t_2) / \tau_2$					$t_H - t_2$			
	0.0001	0.001	0.01	0.1		1 Gyr	1.5 Gyr	2 Gyr	1	10	50	10 ⁷ yr	10 ^{7.5} yr	10 ⁸ yr	10 ^{8.5} yr		
All	36	36	36	36		48	48	48	48	48	48	36	36	36	36		
A	0	12	0	0		6	3	3	4	4	4	9	3	0	0		
	(0%)	(33%)	(0%)	(0%)		(13%)	(6.3%)	(6.3%)	(8.3%)	(8.3%)	(8.3%)	(25%)	(8.3%)	(0%)	(0%)		
B	0	2	10	6		5	8	5	2	9	7	3	14	1	0		
	(0%)	(5.6%)	(28%)	(17%)		(10%)	(17%)	(10%)	(4.2%)	(19%)	(15%)	(8.3%)	(39%)	(2.8%)	(0%)		
C	36	17	23	30		33	33	39	38	32	35	23	15	32	35		
	(100%)	(47%)	(64%)	(83%)		(69%)	(69%)	(81%)	(79%)	(67%)	(73%)	(64%)	(42%)	(89%)	(97%)		
All	9	9	9	9		36	0	0	12	12	12	12	12	12	0		
A	0	6	0	0		6	0	0	2	2	2	3	3	0	0		
	(0%)	(67%)	(0%)	(0%)		(17%)	-	-	(17%)	(17%)	(17%)	(25%)	(25%)	(0%)	-		
B	0	1	2	2		5	0	0	0	3	2	0	4	1	0		
	(0%)	(13%)	(22%)	(22%)		(14%)	-	-	(0%)	(25%)	(17%)	(0%)	(33%)	(8.3%)	-		
C	9	0	5	7		21	0	0	8	6	7	9	4	8	0		
	(100%)	(0%)	(56%)	(78%)		(58%)	-	-	(67%)	(50%)	(58%)	(75%)	(33%)	(67%)	-		

5 Results

5.1 RG fraction

Our method described in section 3 selects 1071 RGs out of the $N = 8857$ parent sample; thus, the RG fraction calculated by simply dividing the number of RGs by the number of all galaxies is about 12%. Considering the volume weight w provided in the MaNGA targeting catalog (Wake et al. 2017) for the Primary+ sample and the secondary sample (ESRWEIGHT), we calculate the intrinsic RG fraction, f_{RG} , as,

$$f_{\text{RG}} = \frac{\sum_{i \in \text{RG}} w_i}{\sum_{i \in \text{All}} w_i}, \quad (10)$$

and obtain $f_{\text{RG}} \simeq 8.1\%$. Furthermore, when restricted to galaxies with $f \sim 0.001$ and considering the completeness discussed in section 4.3, the true RG fraction is $f_{\text{RG}} \sim 12\%$. Note, however, that due to the distribution differences between mock galaxies and real galaxies, it is difficult to estimate the true RG fraction using our results and completeness from the mock data, especially when considering RGs with all f values.

As shown in section 2.2, we have excluded 520 objects as AGN or merging galaxies from the parent sample. If these galaxies have higher f_{RG} than our parent sample, the f_{RG} , including these galaxies, will also be higher than the above value.

5.2 Images and spectra

Figure 12 compares images of the selected RGs constructed from MaNGA datacubes with HSC-SSP PDR3 (Aihara et al. 2022) *gri* composite images. HSC images are deeper and cover a larger area than MaNGA datacubes. We find that although RGs were QGs before rejuvenation, many RGs have a disk structure. The morphologies of RGs will be analyzed in detail in section 5.4.

The upper panels of figure 13 show stacked normalized spectra of current QGs, GVs, and SFGs, separated by whether they are RGs or not; i.e., comparison of rejuvenated QGs (RQGs) with non-rejuvenation QGs (nRQGs), rejuvenating GVs (RGVs) with non-rejuvenation GVs (nRGVs), and rejuvenating SFGs (RSFGs) with non-rejuvenation SFGs (nRSFGs). Then, to compare the spectra of RGs with those of non-rejuvenation galaxies (nRGs), we calculate a normalized residual spectrum, $\Delta F_\lambda(\lambda)$, as,

$$\Delta F_\lambda(\lambda) = \frac{F_{\lambda, \text{RG}}(\lambda) - F_{\lambda, \text{nRG}}(\lambda)}{F_{\lambda, \text{nRG}}(\lambda)}, \quad (11)$$

as shown in the lower panels of figure 13. Additionally, we examine the distribution of galaxies on the well-studied Dn4000 versus the H δ equivalent widths (EW) plane in the lowest panels. We calculate Dn4000 as follows,

$$\text{Dn4000} = \frac{\int_{4000 \text{ \AA}}^{4100 \text{ \AA}} f_\nu d\lambda}{\int_{3850 \text{ \AA}}^{3950 \text{ \AA}} f_\nu d\lambda}. \quad (12)$$

Firstly, it is found that the spectral difference between RGs and non-rejuvenation galaxies is less than the 1σ range, consistent with the previous results from observations by Chauke et al. (2019) and simulated spectra by Zhang et al. (2022). As also mentioned in Zhang et al. (2022), this result suggests that it is difficult to select RGs without an SED fitting method.

Focusing on QGs, panel (a), ΔF_λ is close to 0 for wavelengths longer than 4000 Å, but increases to around 0.1 for shorter wavelengths. This indicates that RQGs have a slightly weaker 4000 Å break than nRQGs. Similarly, in the Dn4000 versus H δ EW plane, RQGs have similar EWs to nRQGs but smaller Dn4000. This is probably due to the presence of a young stellar population, with a smaller Dn4000 value, formed in the rejuvenation event. Also seen is a strong excess in the H α emission line, which also indicates recent star formation.

In the case of GVs, panel (b), ΔF_λ is found to decrease with decreasing wavelength. This is because RGVs retain a larger population of old stars formed before quenching than nRGVs. RGVs have a slightly stronger 4000 Å break than nRGVs, but not as pronounced as in QGs. This tendency is also seen in the Dn4000 versus H δ EW plane, i.e., there is no significant difference in the distributions of RGVs and nRGVs. Looking at ΔF_λ for each line, H recombination lines (Balmer lines) have larger ΔF_λ than the continuum. This is likely because RGVs have stronger Balmer emission lines due to active recent star formation. In contrast, neutral metal lines like NaI $\lambda\lambda 5885, 5889$ (D1, D2 lines) and MgI $\lambda 5175$ have lower ΔF_λ than the continuum, probably because of an aging stellar population formed before quenching.

In the case of SFGs, panel (c), we can see a stronger decreasing trend of ΔF_λ than in GVs. This is because RSFGs have a larger amount of old stellar population formed before quenching than nRSFGs. Similar to GVs, RSFGs have stronger Balmer emission lines and absorption lines of neutral metals than nRSFGs, suggesting the presence of recent star formation and an older stellar population before quenching.

5.3 M^* and SFR distributions

Figure 14 (a) shows that the distribution of RGs in the SFR- M^* plane is biased toward high M^* and SFR values, with their median SFR being higher than those of nRSFGs and nRGVs. We also find that the median M^* of RGs is comparable to that of nRGVs but lower than that

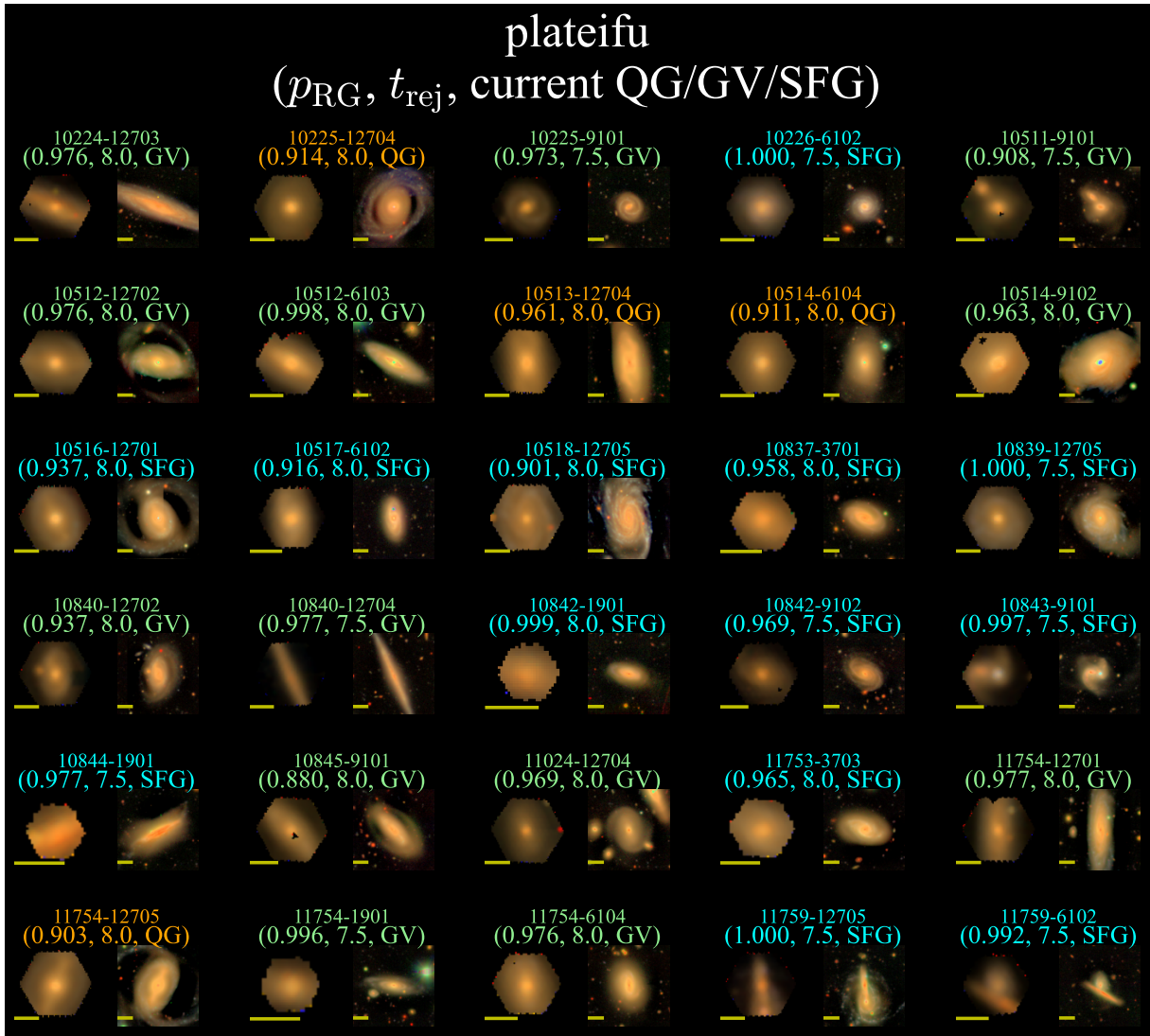


Fig. 12. Cutout images of 30 RGs included in the HSC-SSP PDR3, with their plateifu given at the top. The left side of each panel is a gri image constructed from the MaNGA datacube and the right side is a $1' \times 1'$ HSC gri image. Each image is scaled with the arcsinh method (Lupton et al. 2004). The yellow line in each panel indicates ten arcsecs. For each object, p_{RG} , t_{rej} , and the current state (QG/GV/SFG) are shown below the plateifu, from left to right, with the letters' color corresponding to the current state: orange for QG, yellow-green for GV, and cyan for SFG.

of nRQGs. Note that although RGs have a similar distribution to nRGVs in the 1D distributions of SFR and M^* , the distribution of RGs in the SFR- M^* plane is closer to that of SFGs than of nRGVs, as indicated by the black contours in figure 14 (a).

Figure 14 (a) also gives an insight into the path in the SFR- M^* plane during rejuvenation events. Since we focus on recent rejuvenation events within 10^8 yr (by our definition), even if the sSFR increases to about 10^{-9} yr^{-1} due to rejuvenation, the ratio of the formed mass during the rejuvenation to the total stellar mass is only 10^{-1} . This means that galaxies move upward almost vertically in the SFR- M^* plane by rejuvenation. This result is consistent with Chauke et al. (2019).

Figure 14 (b) shows the distribution of RG fractions in the SFR versus M^* plane. The RG fraction is found to be higher for GVs and massive ($M^* > 10^{11} M_{\odot}$) SFGs. The RG fraction calculated with equation (10) for only galaxies with $M^* > 10^{11} M_{\odot}$ is about 15%, indicating that RGs are more abundant on the high mass side. These results are consistent with previous studies, which compared rejuvenated galaxies with QGs and found that RGs have a smaller mass than QGs (e.g., Chauke et al. 2019; Tacchella et al. 2022).

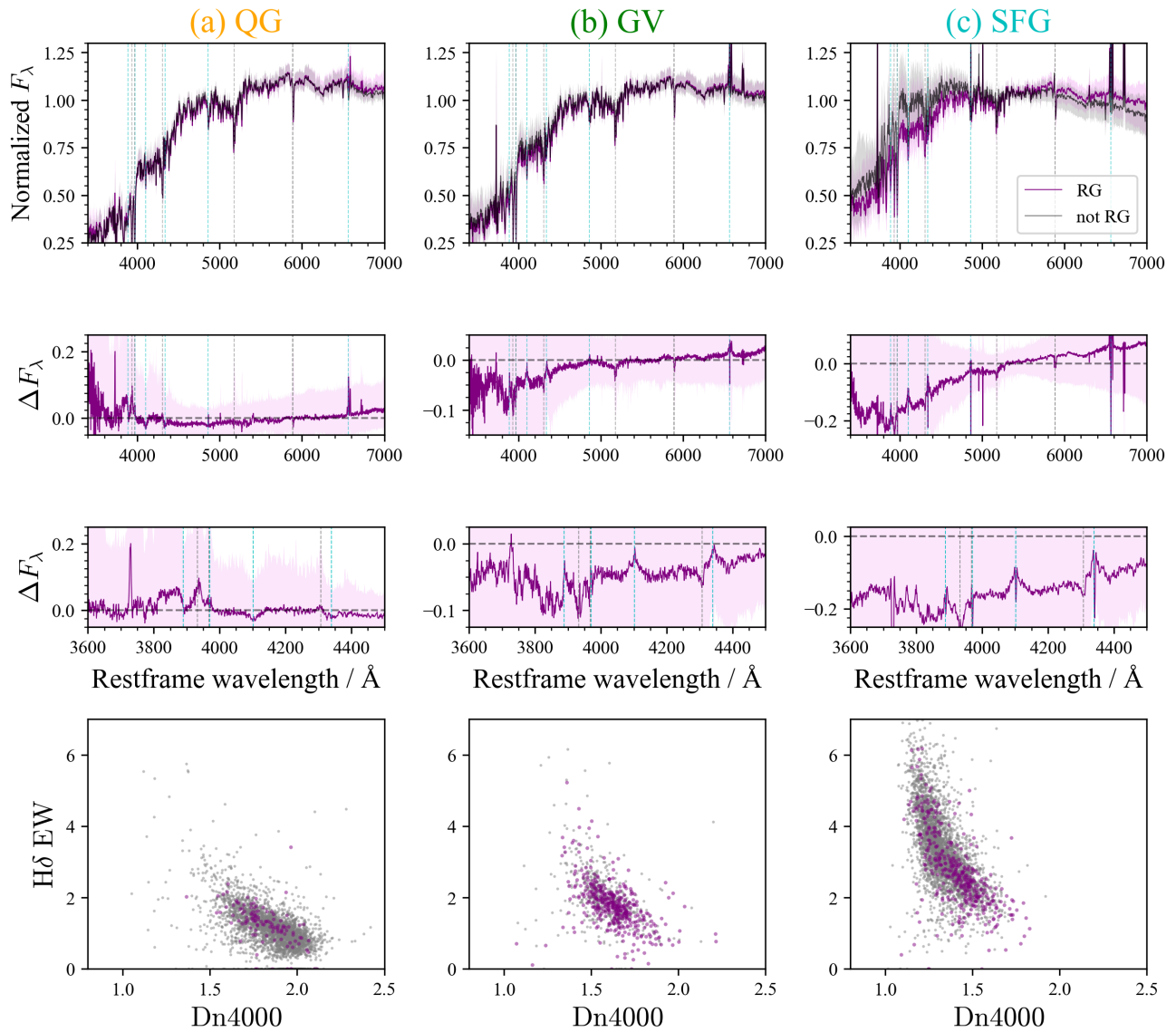


Fig. 13. (Row 1) Stacked normalized spectra $F_{\lambda}(\lambda)$ of QGs (panel [a]), GV (panel [b]), and SFG (panel [c]). The purple and black lines show the spectra of those selected and not selected as RGs, respectively, with shaded areas corresponding to the 1σ confidence intervals. The wavelengths of several strong Balmer lines and neutral metal lines are indicated with cyan and gray dashed lines, respectively. The Balmer lines plotted are from H_{α} to H_{ζ} , from left to right. The metal lines plotted are $\text{Na I } \lambda\lambda 5889, 5885$ (D2 and D1 line), $\text{Mg I } \lambda 5175$, $\text{Ca I } \lambda 4307$ (G line), $\text{Ca II } \lambda 3968$ (H line), and $\text{Ca II } \lambda 3933$ (K line). (Row 2) Differences in the stacked normalized spectra $\Delta F_{\lambda}(\lambda) = \{F_{\lambda, \text{RG}}(\lambda) - F_{\lambda, \text{not RG}}(\lambda)\} / F_{\lambda, \text{not RG}}(\lambda)$ of QGs, GV, and SFG (the order is the same with row 1), where the shaded areas correspond to the 1σ confidence intervals. Similar to row 1, the wavelengths of Balmer lines and neutral metal lines are indicated. (Row 3) Magnified views around 4000 Å. (Row 4) Relationship between $H\delta$ EW and Dn4000. Gray and purple dots indicate nRGs and RGs, respectively.

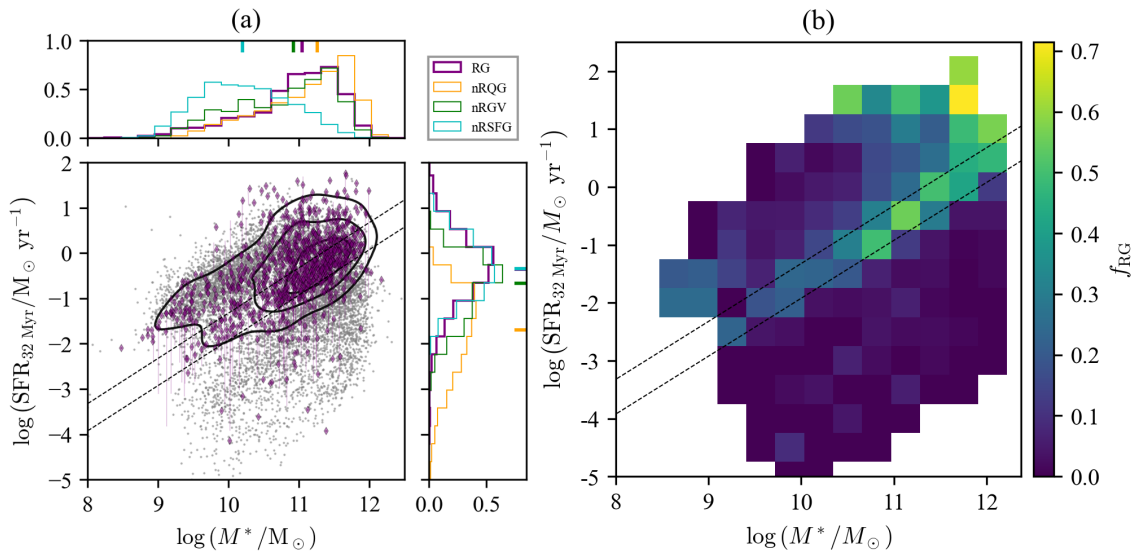


Fig. 14. (a) The distribution of RGs (purple diamonds) in the SFR- M^* plane, with calculated trajectories during the rejuvenation overplotted as solid purple lines (only for randomly selected 100 RGs with $t_{\text{rej}} = 10^{7.5} \text{ yr}$). The dots show all galaxies in our sample, and black solid contours indicate the 1, 2, and 3 σ levels of their distribution. The two black dashed lines correspond to the boundaries of SFG/GV/QG classification at the median redshift of all galaxies. The purple, orange, green, and cyan histograms in the subplots are for RGs, not rejuvenation QGs, not rejuvenation GVs, and not rejuvenation SFGs, respectively. In each subplot, the median of each distribution is indicated by a short bar of the same color as the histogram. (b) The f_{RG} distribution in the SFR- M^* plane. The two black dashed lines correspond to the boundaries of SFG/GV/QG classification at the median redshift of the parent sample. In both panels, we use SFRs in the recent 32 Myr (the most recent age bin).

5.4 Morphologies

In order to compare morphologies between RGs and other galaxies, we show in figure 15 the distributions of the r -band Sérsic index n_r , the r -band effective radius $R_{e,r}$, the bulge-to-total flux ratio B/T , and the ratio of rotational velocity V to velocity dispersion σ , V/σ . For n_r , $R_{e,r}$, and B/T , we use the PyMorph catalog (Domínguez Sánchez et al. 2022), which summarizes photometric morphological parameters obtained from g , r , and i images of MaNGA DR17 galaxies. This PyMorph catalog has two types of results, one fit by a Sérsic profile and the other by a Sérsic+exponential profile, with `FLAG_FIT` parameter indicating which result is reliable: `FLAG_FIT=0` indicates that both fits are reliable; `FLAG_FIT=1` indicates that only the Sérsic fit is successful while the Sérsic+exponential profile fit may not be reliable; `FLAG_FIT=2` indicates that only the Sérsic+exponential fit is successful while the Sérsic profile fit may not be reliable; `FLAG_FIT=3` indicates both fits may be unreliable. Using this parameter, we construct a different sample depending on the morphological parameter to be examined. We use only galaxies with `FLAG_FIT=1` when discussing n_r , only galaxies with `FLAG_FIT=0` or 2 when discussing B/T , and only galaxies with `FLAG_FIT=0`, 1, or 2 when discussing $r_{e,r}$. For the kinematic parameters, V and σ , we use the DAPall catalog (Westfall et al. 2019; Belfiore et al. 2019).

First, we focus on the photometric morphology param-

eters. From figure 15 (a) and (b), we find that RGs have a very different morphology from nRQGs (the p -value of Kolmogorov-Smirnov test is $p \ll 0.05$); RGs show more a disk-like morphology (lower n_r and B/T) than nRQGs and a more elliptical-like morphology (higher n_r) than nRSFGs. From figure 15 (c), we find that RGs tend to have a larger radius than nRSFGs and a smaller radius than nRQGs. Similar to the n_r and B/T distributions, RGs have almost the same $R_{e,r}$ distribution as nRGVs. Based on the above results, we conclude that the RGs have a photometric parameter distribution between nRQGs and nRSFGs, similar to nRGVs.

We can also see similar trends in the kinematic morphology parameters. Figure 15 (d) shows that RGs have an intermediate distribution of V/σ between nRSFGs and nRQGs. Particularly, RGs have a more rotation-supported morphology than nRQGs, even though the mass distribution of nRQGs is not significantly different from that of the RGs. RGs also show a similar V/σ distribution to nRGVs, but nRGVs have a slightly more rotational-supported than RGs.

5.5 Environment

To examine the environmental dependence of RGs, we cross-match our parent sample with the group catalog of Tempel et al. (2012) that applied a modified friends-of-

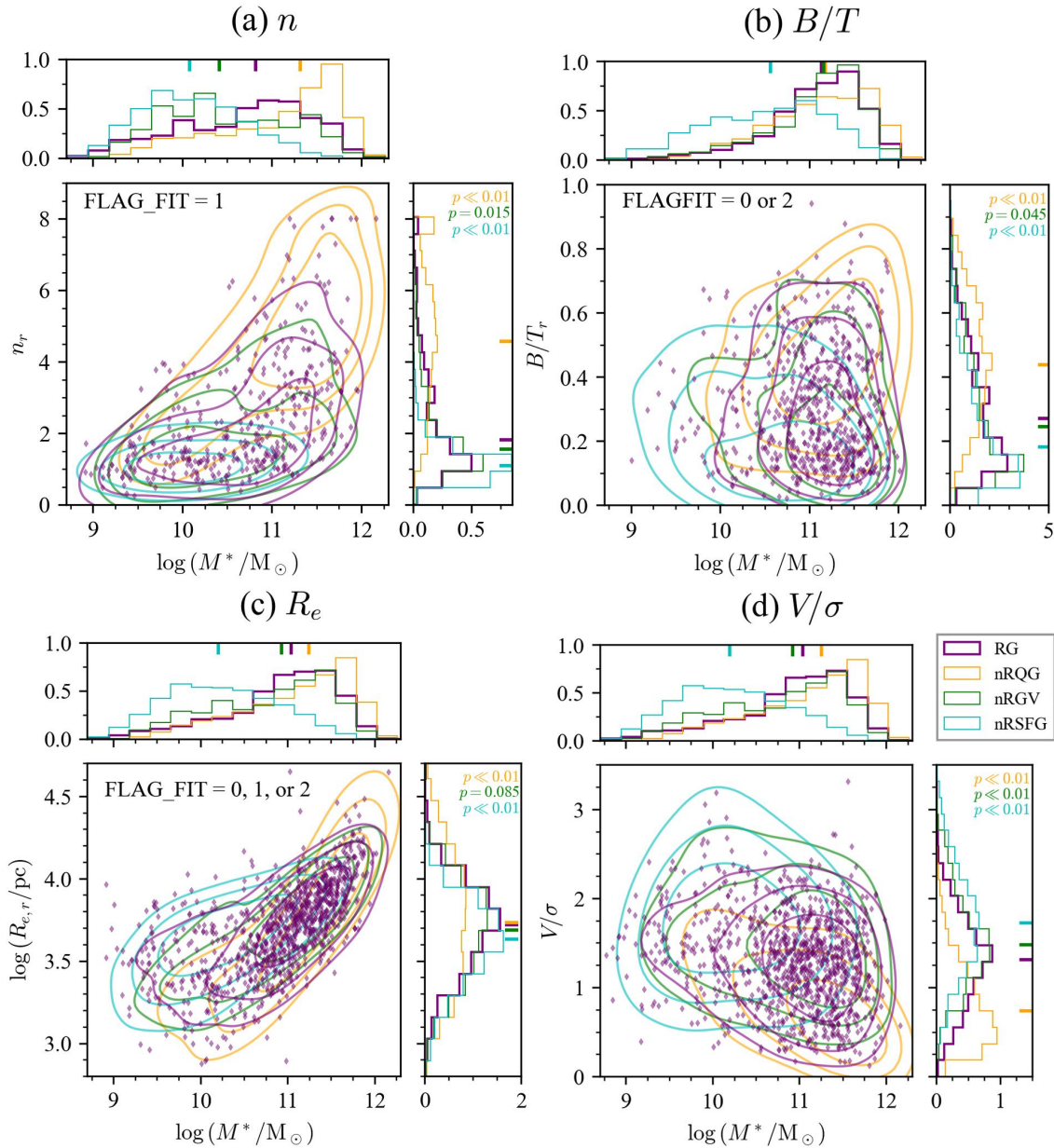


Fig. 15. The relationship between stellar mass and four indices of morphology: Sérsic index in the r band n_r (panel [a]), bulge to total flux ratio B/T ([b]), effective radius in the r band $r_{e,r}$ ([c]), the ratio of the rotation velocity V to the velocity dispersion σ ([d]). Plotted in panels (a), (b), and (c) are only galaxies with $\text{FLAG_FIT}=1$, $\text{FLAG_FIT}=0$ or 2 , and $\text{FLAG_FIT}=0, 1$, or 2 . In each panel, purple, orange, green, and cyan colors indicate RGs, nRQGs, nRGVs, and nRSFGs, respectively, where dots are individual objects, contours are the 0.5 , 1 , and 2σ levels of the distribution, and histograms are the distributions of individual parameters, with medians indicated by short bars. Shown in the top right of each y -axis histogram are the p -values of the Kolmogorov–Smirnov test between the RG sample and the three non-rejuvenation galaxy samples (nQGs, nGVs, nSFGs).

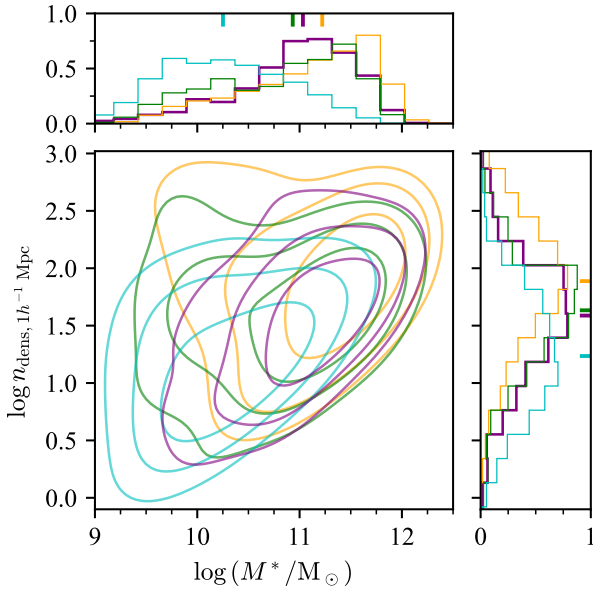


Fig. 16. Same as Figure 15, but for stellar mass versus the scaled environmental density within $1h^{-1}$ Mpc from each galaxy. Individual galaxies are not plotted.

friends method to the SDSS DR8, obtaining 7585 galaxies with environmental information. We consider those with the richness $n_{\text{rich}} = 1$ to be in the field or void environment, while those with $n_{\text{rich}} > 4$ to be in the cluster environment.

Figure 16 compares among galaxy types the distribution of normalized environmental densities within $r = 1h^{-1}$ Mpc that are calculated by Tempel et al. (2012) from galaxy luminosity density fields in the same manner as Liivamägi et al. (2012). We find that the density distribution of RGs is intermediate between those of QGs and SFGs, being similar to GVs. This trend is similar to the morphology trend found in section 5.4 and consistent with previous studies such as Schawinski et al. (2007); Thomas et al. (2010); Chauke et al. (2019) in that RGs tend to be in lower-density environments than QGs.

Next, we draw a phase space diagram (Bertschinger 1985) for galaxies in the cluster environment ($n_{\text{rich}} > 4$), with the clustocentric radius r_{sep} normalized by virial radius r_{vir} being the horizontal axis and the clustocentric velocity in the line-of-sight direction v_{LOS} normalized the velocity dispersion in the cluster σ_{cl} being the vertical axis, using the group catalog by Tempel et al. (2012). Following Rhee et al. (2017), we classify galaxies into five regions, A, B, C, D, and E, according to their positions on the phase-space diagram as shown in figure 17. Rhee et al. (2017) have reported that region A is dominated by interlopers and galaxies that have fallen into the cluster recently. In contrast, region E is dominated by galaxies that have been in the cluster for a long time.

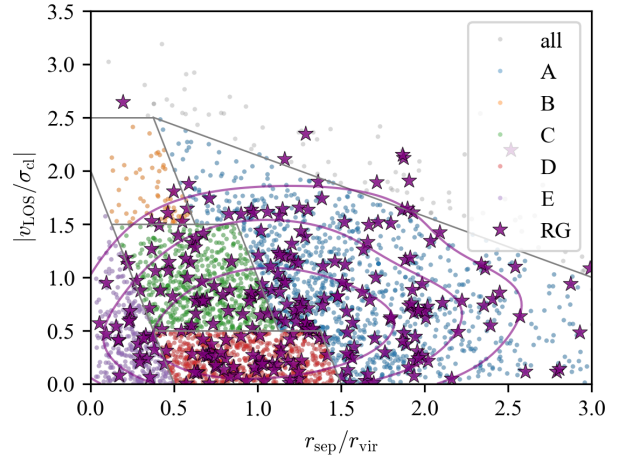


Fig. 17. The phase-space diagram of our galaxies in the cluster environment. Following Rhee et al. (2017), we divide the cluster environment into five regions (A to E) whose boundaries are shown by solid gray lines. Dots indicate all galaxies, color-coded according to the region they reside in. Purple stars are RGs, and purple contours are the 1 and 2σ levels of their distribution.

Table 4 shows f_{RG} for the five regions and the field. We find that f_{RG} is higher in region A and the field than in regions B-D and E. We also calculate $f_{\text{RG/nRQG}}$, the ratio of the number of RGs to the number of nRQGs. As RGs were QGs before rejuvenation, we consider $f_{\text{RG/nRQG}}$ as an indicator of the fraction of QGs that caused rejuvenation, i.e., how likely rejuvenation occurs in QGs. $f_{\text{RG/nRQG}}$ is found to be highest in the field and decreases toward the cluster center in the order of regions A, B-D, and E. This suggests that rejuvenation is more likely to occur in galaxies in the field and galaxies that have just entered a cluster than in galaxies that have been in a cluster for a long time.

6 Discussion

6.1 RGs are important players in galaxy evolution

One of the key questions in the study of rejuvenation is the importance of RGs in galaxy evolution, especially how much of the total stellar mass was formed by rejuvenation and whether or not rejuvenation has a significant contribution to cosmic star formation. Chauke et al. (2019) have reported that about 10% of the total stellar mass of rejuvenated galaxies is formed in the rejuvenation event and that RGs contribute only about 0.3% of the cosmic SFR density (CSFRD) over $z \sim 0.7 - 1.5$. Tacchella et al. (2022) have reported that, at most, only about 10% of the total mass is formed in rejuvenation events.

To address this question, first, we calculate C_j , the contribution of each current galaxy population j ($j = \text{nRSFG, nRGV, nRQG, and RG}$) to the CSFRD in the last 100

Table 4. The number of each type of galaxies for each environment. The error in the fraction only includes the Poisson error.

	Number					Fraction	
	All	RG	nRSFG	nRGV	nRQG	$f_{\text{RG}}: \text{RG}/\text{All}$	$f_{\text{RG}/\text{nRQG}}: \text{RG}/\text{nRQG}$
All Environment	6743	731	2831	376	2805	$10.8 \pm 0.4\%$	$26.1 \pm 1.1\%$
Field ($N_{\text{rich}} = 1$)	2063	221	1179	122	541	$10.7 \pm 0.8\%$	$40.9 \pm 3.3\%$
A	1056	129	362	65	500	$12.2 \pm 1.1\%$	$25.8 \pm 2.5\%$
Cluster ($N_{\text{rich}} > 4$)	1294	102	326	69	797	$7.9 \pm 0.8\%$	$12.8 \pm 1.3\%$
B-D	1294	102	326	69	797	$7.9 \pm 0.8\%$	$12.8 \pm 1.3\%$
E	272	20	38	13	201	$7.4 \pm 1.7\%$	$10.0 \pm 2.3\%$

Myr, the timescale of rejuvenation in our definition. Here, C_j is defined as the ratio of the total M^* formed in j -type galaxies in the last 100 Myr to the total M^* formed in all galaxies in the last 100 Myr,

$$C_j = \frac{\sum_{i \in j} w_i M_{i,100 \text{ Myr}}^*}{\sum_{i \in \text{All}} w_i M_{i,100 \text{ Myr}}^*},$$

where $M_{i,100 \text{ Myr}}^*$ is the formed stellar mass in a galaxy i in the last 100 Myr and w_i is the volume weight of this galaxy given in the MaNGA catalog. The mass dependence of C_j is shown in the upper figure 18. The sum of C_{RG} for all M^* bins is about 17%, meaning that RGs contribute about 17% to the CSFRD in the recent 100 Myr, about two orders of magnitude larger than the value obtained by Chauke et al. (2019) for rejuvenated galaxies at $z \sim 0.8$. If the detail of rejuvenation events is similar at $z \sim 1$ and $z \sim 0$, this result implies that rejuvenation events have higher importance at lower z . However, this difference may be explained by the difference in the definition of rejuvenation and the difference in the parent sample (they search for RGs only from QGs). It may also be attributed to the z dependence of the CSFRD because the CSFRD at $z \sim 1$ is about one order of magnitude higher than at $z \sim 0$ (e.g., Madau & Dickinson 2014). Note also that we cannot rule out the possibility that C_j is overestimated or underestimated in this study due to the contamination or completeness discussed in section 4.3.

Next, we calculate μ , the ratio of the formed stellar mass in the last 100 Myr, $M_{100 \text{ Myr}}^*$, to the total stellar mass M^* for each RG (same as the discussion in section 4.2). The lower panel of figure 18 shows μ as a function of M^* . We find that rejuvenation events increase M^* only by a few percent at most, with $\sim 0.1\%$ on average. This result roughly agrees with Akhshik et al. (2021) reporting that 0.5% of M^* is formed in 100-Myr-timescale rejuvenation events at $z = 1.883$. This agreement may suggest that the detail of rejuvenation events does not change with redshift.

Note that the values of μ obtained here are consistent with the result for mock data presented in section 4.2 that our method can select galaxies with $\mu \sim 10^{-3}$ with high completeness. This consistency suggests that our RG sample is not significantly contaminated. On the other hand,

we cannot rule out the possibility that $\mu \sim 10^{-3}$ is obtained just because our method fails to select RGs with other μ values. To do a more solid statistical discussion, it will be important to evaluate contamination and completeness using a larger mock sample covering wider parameter ranges or maybe cosmological simulation data and to develop a more robust selection method.

The very small increase in M^* by rejuvenation obtained here is primarily because the rejuvenation timescale, 100-Myr, is too short to increase M^* significantly. However, if galaxies experienced rejuvenation events many times in the past, rejuvenation may be an important channel of galaxy mass growth. Although we cannot directly detect such past rejuvenation events for our sample because of insufficient time resolution of the reconstructed SFHs, we discuss the possibility of multiple rejuvenation events in section 6.2.

6.2 Multiple rejuvenation scenario

Whether rejuvenation can occur more than once in a galaxy's lifetime is still unclear. Nelson et al. (2018) have found that $\sim 10\%$ and $\sim 1\%$ of massive passive galaxies in the TNG100 simulation have experienced one and more than one rejuvenation event, respectively. In this subsection, we roughly estimate N_{rej} , the number of times galaxies have experienced rejuvenation, using f_{RG} obtained in section 5.1.

We simply assume that f_{RG} is $\sim 8\%$ (the value obtained in section 5.1) over $z \sim 0 - 1$. This assumption comes from the fact that previous studies of $z \lesssim 1$ galaxies have obtained similar f_{RG} values (Tacchella et al. 2022; Chauke et al. 2019). We also estimate the timescale of rejuvenation τ_{rej} , the time from restarting star formation to stopping the resumed star formation, to be $\tau_{\text{rej}} (10^8 \text{ yr} - 10^{7.5} \text{ yr}) / 0.21 \sim 320 \text{ Myr}$ because about 21% of the RGs with $t_{\text{rej}} = 10^8 \text{ yr}$ returned to QGs at $10^{7.5} \text{ yr}$. Note that this calculation implicitly assumes a constant probability that the resumed star formation will end within a certain time.

With these assumption and estimate, the averaged N_{rej}

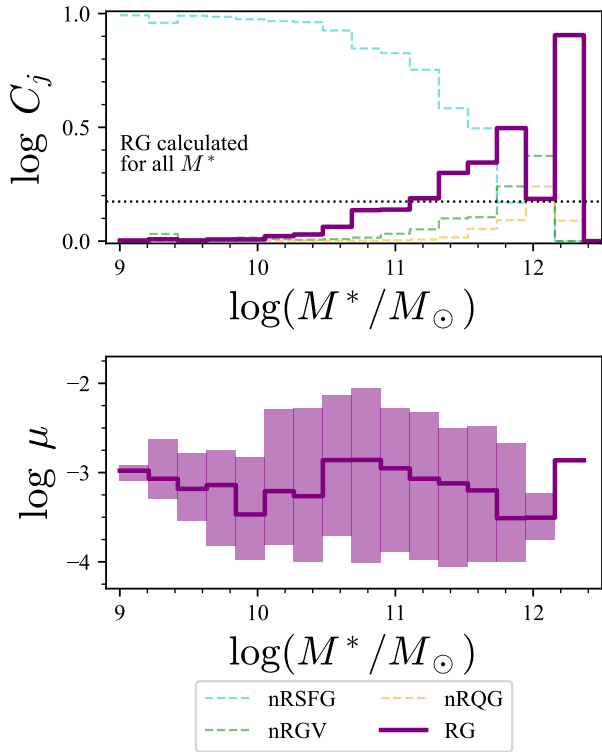


Fig. 18. *Upper panel.* Distribution of C_j as a function of M^* for four types of galaxies coded by color. The horizontal dotted line indicates C_{RG} , the contribution of RGs averaged over all masses. *Lower panel.* μ (purple solid line) and its 1σ confidence level (purple shaded area) as a function of M^* .

for all galaxies between $z \sim 0 - 1$ can be calculated as $N_{\text{rej}} = (t|_{z=1} - t|_{z=0}) f_{\text{RG}} / \tau_{\text{rej}} \sim 2.1$, suggesting that galaxies have experienced rejuvenation twice at $z \lesssim 1$ on average. Because f_{RG} increases with stellar mass as shown in figure 14, massive galaxies can have larger N_{rej} . For example, the N_{rej} of $M^* > 10^{11} M_{\odot}$ galaxies, with $f_{\text{RG}} \sim 18\%$, can be as high as $N_{\text{rej}} \sim 4.4$, meaning that such massive galaxies are likely to have experienced multiple rejuvenation events.

As shown in figure 14, the path of a rejuvenation event in the SFR- M^* plane is almost a vertical ascent. Considering that the time scale of rejuvenation is $\tau_{\text{rej}} \sim 0.3$ Gyr and that rejuvenation may occur many times, essentially all rejuvenation events have to end up with re-quenching. Therefore, we infer that massive galaxies are frequently moving up and down on the massive side of the SFR- M^* plane.

To verify whether rejuvenation can occur many times, we use the reconstructed SFHs of current QGs to calculate the time from the last quenching t_{iq} , the time since the galaxy last entered the QG regime from the SFG or GV regime. In this verification, we consider two patterns of quenching, “long quenching” and “mini quenching”.

In the “long quenching”, it is assumed that galaxies

never (at least for a longer time than τ_{rej}) rejuvenate once quenched. This corresponds to the popular galaxy evolution scenario in that SFGs become QGs. For simplicity, we assume that the probability of “long quenching” for SFGs does not change with cosmic time. This assumption is reasonable because the cosmological evolution of quenching possibility can be ignored for our focusing timescale; e.g., if an observed object has $z \sim 0.03$, even the second-to-last age bin only reaches about $z \sim 0.2$, and the quenching rate at $z \sim 0.2$ is about only two times higher than that at $z \sim 0.03$ according to Peng et al. (2010).

In contrast, “mini quenching” is temporary quenching that is terminated by rejuvenation. Recently, Dome et al. (2023); Looser et al. (2023b) have reported that high- z (low-mass) galaxies can experience mini-quenching. Dome et al. (2023) have found the duration of a mini-quenching event to be 20 – 40 Myr at $z \sim 7$, being comparable to the dynamical time of galaxies at this redshift. Because the dynamical time scales as $t_{\text{dyn}} \propto \rho^{-1/2} \propto (1+z)^{-3/2}$, we expect the duration of a mini-quenching event of local galaxies to be $\sim 400\text{--}900$ Myr, which is indeed similar to the rejuvenation timescale τ_{rej} of our RGs. If galaxies can have multiple rejuvenation events, quenching other than the last mini quenching (i.e., the long quenching and the previous mini quenchings) will not be reflected in t_{iq} because t_{iq} only focuses on the last quenching event. Therefore, the distribution of t_{iq} is expected to have an excess on a shorter time scale than τ_{rej} .

In the histogram of t_{iq} and the number normalized by the duration of those time bins shown in figure 19, we indeed find an excess with $t_{\text{iq}} \lesssim \tau_{\text{rej}}$. This excess can be explained by considering that the information on mini-quenching that occurred at $t_{\text{iq}} \gtrsim \tau_{\text{rej}}$ is overwritten by rejuvenation and the next mini-quenching and hence that only mini-quenching at $t_{\text{iq}} \lesssim \tau_{\text{rej}}$ contributes to the histogram. However, this interpretation is inconsistent with the fact that rejuvenation occurs at $z > 0$ as well, e.g., $z \sim 0.8$ (Chauke et al. 2019; Tacchella et al. 2022) and $z = 1.88$ (Akhshik et al. 2021). We conclude that galaxies, especially massive ones, have likely experienced multiple rejuvenation events.

6.3 Why are they disk-like?

As shown in figures 15 (a) and (c), RGs have a more disk-like or rotational-supported morphology distribution than nRQGs, even though RGs were QGs before rejuvenation by definition. In this section, we discuss the reason for this morphological difference between RGs and the nRQGs. Here, we propose the following two hypotheses to explain the disk-like structure of RGs.

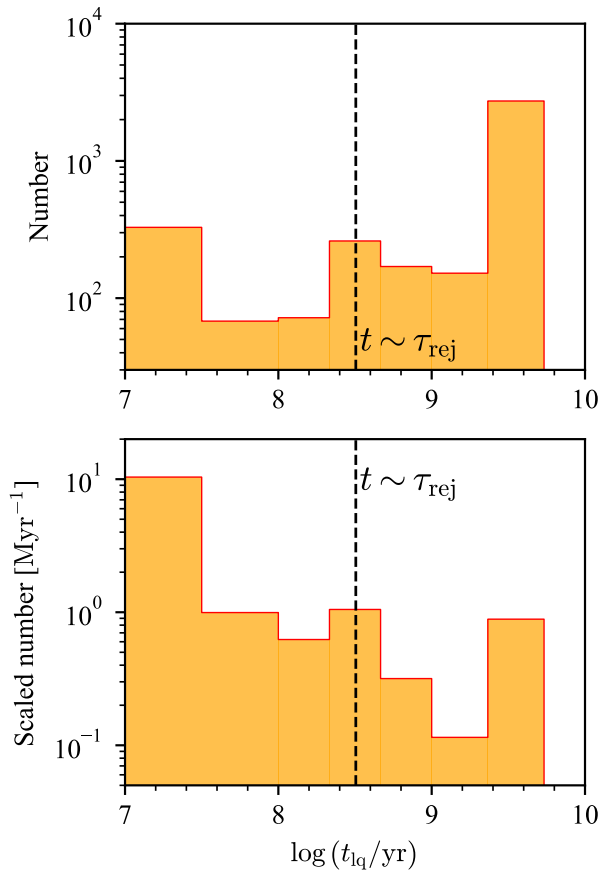


Fig. 19. The distribution of t_{lq} . The upper panel plots the number of RGs falling into each t_{lq} bin while the lower panel plots a scaled number, i.e., the number divided by the bin width. Vertical black dashed lines indicate $t_{lq} = \tau_{rej}$.

1. Selective rejuvenation (SR)

As high as one-third (= 1259/3806) of the QGs in our sample have disk-like morphology, i.e., $V/\sigma > 1$. Furthermore, it is well known that some spiral galaxies are anemic spirals without star formation (e.g., van den Bergh 1976; Shimakawa et al. 2022). Fudamoto et al. (2022) have found the reddest spiral galaxies at $z \sim 1 - 3$ from JWST/NIRCam images and reported that one of them is well-described as a passive galaxy. If only disk-like QGs, or passive spiral galaxies, can rejuvenate, and if their morphology does not change during rejuvenation, then RGs will have a disk-like morphology. This is “selective” rejuvenation, where only disk-like QGs can rejuvenate.

2. Disk-forming rejuvenation (DR)

The disk-like morphology distribution can be explained if elliptical-like QGs form a disk during rejuvenation. This scenario does not prohibit the presence of RGs that evolved from disk-like QGs.

We argue that the DR scenario is unlikely because of two

serious problems. First, it is extremely difficult to change morphology in a short period of $\tau_{rej} \sim 320$ Myr. Although Diaz et al. (2018) claim that elliptical galaxies can form a disk by merging with gas-rich satellite galaxies, it takes a Gyr time scale, much longer than τ_{rej} . Besides, as shown in figure 14, galaxies increase the stellar mass only by $\sim 0.1\%$ in a single rejuvenation event. It is challenging to make a noticeable disk with such a small amount of mass increase. Second, there are significant differences in morphologies between RGs and nRQGs (figure 15). These differences, especially in kinetics morphology V/σ , may not be explained by simple star formation in the outer part of galaxies due to rejuvenation. For these reasons, we conclude that the DR scenario is unlikely.

We then test the SR scenario using the M^* and $n_{dens,1h-1 \text{ Mpc}}$ plane. As shown in figure 14, M^* does not change significantly before and after rejuvenation. Because $n_{dens,1h-1 \text{ Mpc}}$ should be almost unchanged before and after rejuvenation, the spatial distribution of RGs and their progenitors in this plane should be the same. By comparing the distribution of RGs, disk-like nRQGs, and elliptical nRQGs, we can test the SR scenario.

In the SR scenario, only disk-like QGs are the progenitors of RGs. Because not all disk-like QGs may be able to rejuvenate, the distribution of disk-like QGs does not necessarily have to be the same as of RGs. However, the distribution of disk-like QGs must cover that of RGs. In contrast, elliptical QGs can take a significantly different distribution from RGs.

Figure 20 shows the M^* and $n_{dens,1h-1 \text{ Mpc}}$ distributions of RGs, disk-like nRQGs, and elliptical nRQGs. Here, we define galaxies with the same V/σ distribution with RGs as disk-like nRQGs and construct a sample of disk-like nRQGs by selecting an nRQG with the nearest V/σ for each RG. On the other hand, we define galaxies with $V/\sigma < 0.5$ as elliptical nRQGs. We find that all RGs are within the area where disk-like nRQGs are found, while a significant fraction of RGs are outside the area where elliptical nRQGs are found. This result is consistent with the SR scenario. Note that this result does not rule out the existence of RGs that evolved from elliptical-like QGs. An interesting feature in this figure is that the distribution of disk-like nRQGs has a secondary peak around $\log(M^*/M_\odot) \sim 10$ and $\log(n_{dens,1h-1 \text{ Mpc}}) \sim 2.5$ where no RGs exist. This may imply that low-mass sources in high-density regions cannot rejuvenate, consistent with the discussion in section 5.5. In a subsequent paper, we will further discuss the mechanism of rejuvenation, including the conditions in which rejuvenation occurs.

Finally, we propose further tests for the two scenarios focusing on the mechanisms expected in these scenarios.

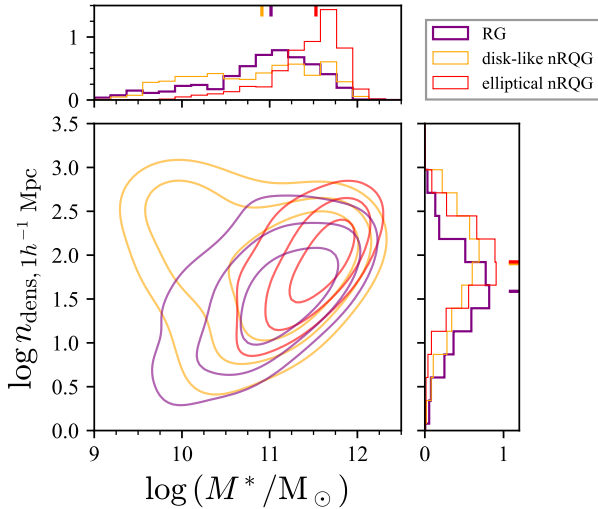


Fig. 20. Same as Figure 16, but for RGs (purple), disk-like nRQGs (orange), and elliptical nRQGs (red).

One possible mechanism with the SR scenario is that the remaining gas in disk-like QGs is used for rejuvenation. In this case, disk-like QGs must have a higher molecular gas fraction f_{gas} than normal QGs, and the star formation in RGs must be driven by an increase in star formation efficiency (SFE). Another possible mechanism in the SR scenario is that gas-poor disk-like QGs obtain gas to restart star formation. In this case, we expect lower or similar f_{gas} in disk-like QGs. In any case, the SR scenario can be tested using a combination of f_{gas} and SFE data. Additionally, the two scenarios can be verified by analyzing the spatially resolved SFH and kinetics of gases in RGs; e.g., evidence of gas inflows suggests the DR scenario. Thus, a specially-resolved discussion of f_{gas} , SFE, and kinetics using radio observation like ALMA and IFU data from MaNGA will help us constrain the mechanism and verify the SR and DR scenarios. These hypotheses can also be tested by using simulation data to examine the progenitors of the RGs.

6.4 The contribution of AGN

In this study, we exclude 520 objects in section 2.2 as AGN or merging galaxies. This number amounts to only 6% of the size of the parent sample and also smaller than the number of selected RGs. Therefore, AGN activities as detected in MaNGA data are unlikely to be the primary driver of rejuvenation. Note, however, that the parent sample may have some undetected AGNs and merging sources. It is also possible that past AGN activities or mergers that are not detected from current observations could trigger rejuvenation because rejuvenation started $10^{7.5}$ yr or 10^8 yr ago.

7 Conclusion

In this paper, we have presented the HINOTORI project that aims at understanding the nature of RGs using the SFH. As the first step of this project, we have performed a flexible SED fitting analysis using PROSPECTOR on 8857 MaNGA galaxies with photometric and spectroscopic data and constructed a sample of 1071 RGs, the largest ever SFH-selected RG sample. Our main results are summarized as follows:

- Tests with mock data show that our selection method can select $f \sim 0.001$ RGs with high completeness ($\sim 67\%$).
- The RG fraction is $f_{\text{RG}} = 8.1\%$ after volume-weight correction. The selected RGs contribute $\sim 20\%$ of the CSFRD in the recent 100 Myr.
- From a rough estimate of N_{rej} , we find that single galaxies can rejuvenate multiple times. Multiple rejuvenations may significantly contribute to the mass assembly of galaxies, while a single rejuvenation increases the stellar mass only $\sim 0.1\%$.
- RGs have more disk-like morphology than nRQGs, suggesting the “selective rejuvenation” scenario where disk-like QGs rejuvenate more likely than elliptical QGs.

The next goal of HINOTORI is to specify the mechanism of rejuvenation. We plan to analyze the IFU data of the selected RGs in the future. Using simulation data is also an effective way to constrain the rejuvenation mechanism. Furthermore, radio observations of molecular gas with, e.g., ALMA will allow us to discuss the star formation activity in RGs in more detail. We also plan to examine the relationship between AGN activity and rejuvenation (c.f., Martin-Navarro et al. 2022).

Recent studies have found high- z low- M^* QGs ($M^* \sim 5 \times 10^8 M_\odot$ at $z \sim 7.3$, Looser et al. 2023a) and post-starburst galaxies ($M^* \sim 4 \times 10^7 M_\odot$ at $z \sim 5.2$, Strait et al. 2023) in JWST data. These findings may imply that high- z low-mass QGs evolve into more massive galaxies at lower z through repeated rejuvenation events (c.f., Looser et al. 2023a; Strait et al. 2023; Dome et al. 2023). To evaluate the importance and the role of rejuvenation in galaxy evolution, we have to explore RGs in a wide redshift range. Besides, the z -dependence of f_{RG} will place stronger constraints on the possibility of multiple rejuvenations. High- z RG exploration needs a deep infrared spectroscopic survey with such as JWST/NIRSpec, TAO/SWIMS, Roman/WFI, and Euclid/NISP. The development of a low-cost RG selection method (e.g., Zhang et al. 2022) is another effective way to select RG candidates for follow-up spectroscopic observation and advance RG research. As our results with mock data suggest, the out-

shining problem is serious when we reconstruct the SFHs of galaxies with strong rejuvenation. Spatial resolved (or pixel-by-pixel) SED fitting may be able to solve this problem as Sorba & Sawicki (2018) and Giménez-Arteaga et al. (2023) suggested.

Acknowledgments

We thank Keiya Hirashima and Kazunari Iwasaki for giving us useful advice for using a high-performance computing system.

This work is partly supported by the 2022 Undergraduate Research Abroad in Science Program of School of Science, the University of Tokyo. We thank Roberto Maiolino and other members of the Galaxy Formation and Evolution Group at Kavli Institute for Cosmology, Cambridge (KICC) for fruitful discussion in group meetings and with a cup of coffee.

This research is partially supported by Initiative on Promotion of Supercomputing for Young or Women Researchers, Supercomputing Division, Information Technology Center, The University of Tokyo. Numerical computations were in part carried out on Small Parallel Computers at Center for Computational Astrophysics, the National Astronomical Observatory of Japan, iDark cluster at Kavli Institute for the Physics and Mathematics of the Universe, The University of Tokyo, and the Fujitsu PRIMERGY CX400M1/CX2550M5 (Oakbridge-CX) at the Information Technology Center, The University of Tokyo.

TT is supported by Forefront Physics and Mathematics Program to Drive Transformation (FoPM), a World-leading Innovative Graduate Study (WINGS) Program, the University of Tokyo. H.Yesuf was supported by JSPS KAKENHI Grant Number JP22K14072 and the Research Fund for International Young Scientists of NSFC (11950410492).

Funding for the Sloan Digital Sky Survey IV has been provided by the Alfred P. Sloan Foundation, the U.S. Department of Energy Office of Science, and the Participating Institutions. SDSS acknowledges support and resources from the Center for High-Performance Computing at the University of Utah. The SDSS web site is www.sdss4.org.

SDSS is managed by the Astrophysical Research Consortium for the Participating Institutions of the SDSS Collaboration including the Brazilian Participation Group, the Carnegie Institution for Science, Carnegie Mellon University, Center for Astrophysics — Harvard & Smithsonian (CfA), the Chilean Participation Group, the French Participation Group, Instituto de Astrofísica de Canarias, The Johns Hopkins University, Kavli Institute for the Physics and Mathematics of the Universe (IPMU) / University of Tokyo, the Korean Participation Group, Lawrence Berkeley National Laboratory, Leibniz Institut für Astrophysik Potsdam (AIP), Max-Planck-Institut für Astronomie (MPIA Heidelberg), Max-Planck-Institut für Astrophysik (MPA Garching), Max-Planck-Institut für Extraterrestrische Physik (MPE), National Astronomical Observatories of China, New Mexico State University, New York University, University of Notre Dame, Observatório Nacional / MCTI, The Ohio State University, Pennsylvania State University, Shanghai Astronomical Observatory, United Kingdom Participation Group, Universidad Nacional Autónoma de México, University of Arizona, University of Colorado

Boulder, University of Oxford, University of Portsmouth, University of Utah, University of Virginia, University of Washington, University of Wisconsin, Vanderbilt University, and Yale University.

The Hyper Suprime-Cam (HSC) collaboration includes the astronomical communities of Japan and Taiwan, and Princeton University. The HSC instrumentation and software were developed by the National Astronomical Observatory of Japan (NAOJ), the Kavli Institute for the Physics and Mathematics of the Universe (Kavli IPMU), the University of Tokyo, the High Energy Accelerator Research Organization (KEK), the Academia Sinica Institute for Astronomy and Astrophysics in Taiwan (ASIAA), and Princeton University. Funding was contributed by the FIRST program from the Japanese Cabinet Office, the Ministry of Education, Culture, Sports, Science and Technology (MEXT), the Japan Society for the Promotion of Science (JSPS), Japan Science and Technology Agency (JST), the Toray Science Foundation, NAOJ, Kavli IPMU, KEK, ASIAA, and Princeton University.

This paper is based on data collected at the Subaru Telescope and retrieved from the HSC data archive system, which is operated by the Subaru Telescope and Astronomy Data Center (ADC) at NAOJ. Data analysis was in part carried out with the cooperation of Center for Computational Astrophysics (CfCA), NAOJ. We are honored and grateful for the opportunity of observing the Universe from Maunakea, which has the cultural, historical and natural significance in Hawaii.

Appendix. Comparison of PROSPECTOR's outputs with existing SED fitting results

Several studies have estimated galaxy parameters for the MaNGA sample with SED fitting, although their results cannot be used to select RGs because they are based on parametric SFHs. In this subsection, to further demonstrate the validity of our SED fitting results with PROSPECTOR, we compare the estimated basic parameters with existing SED fitting results in the Pipe3D DR17 catalog (Sánchez et al. 2022). This catalog summarizes the results of a stellar population and ionized gas analysis of the MaNGA data set using the pyPipe3D pipeline (Lacerda et al. 2022). Note that the true values of individual parameters, like assumed mock values in section 4.1, are unavailable and hence that we cannot know which SED fitting results are closest to the truth. However, we expect our results to be generally consistent with the values in the Pipe3D catalog.

The Pipe3D catalog has two types of SFR; $\log_{\text{SFR}}_{\text{ssp}}$ obtained from simple stellar population analysis and $\log_{\text{SFR}}_{\text{Ha}}$ obtained from the Ha flux. We use both SFRs in the Pipe3D catalog in the comparison. Lines 1 and 2 of figure 21 show that the SFRs estimated with PROSPECTOR strongly correlate with those from the Pipe3D catalog for GVs and SFGs. Indeed, Spearman's correlation coefficient calculated for all galaxies is $\rho \simeq 0.75$ for SSP-based SFRs

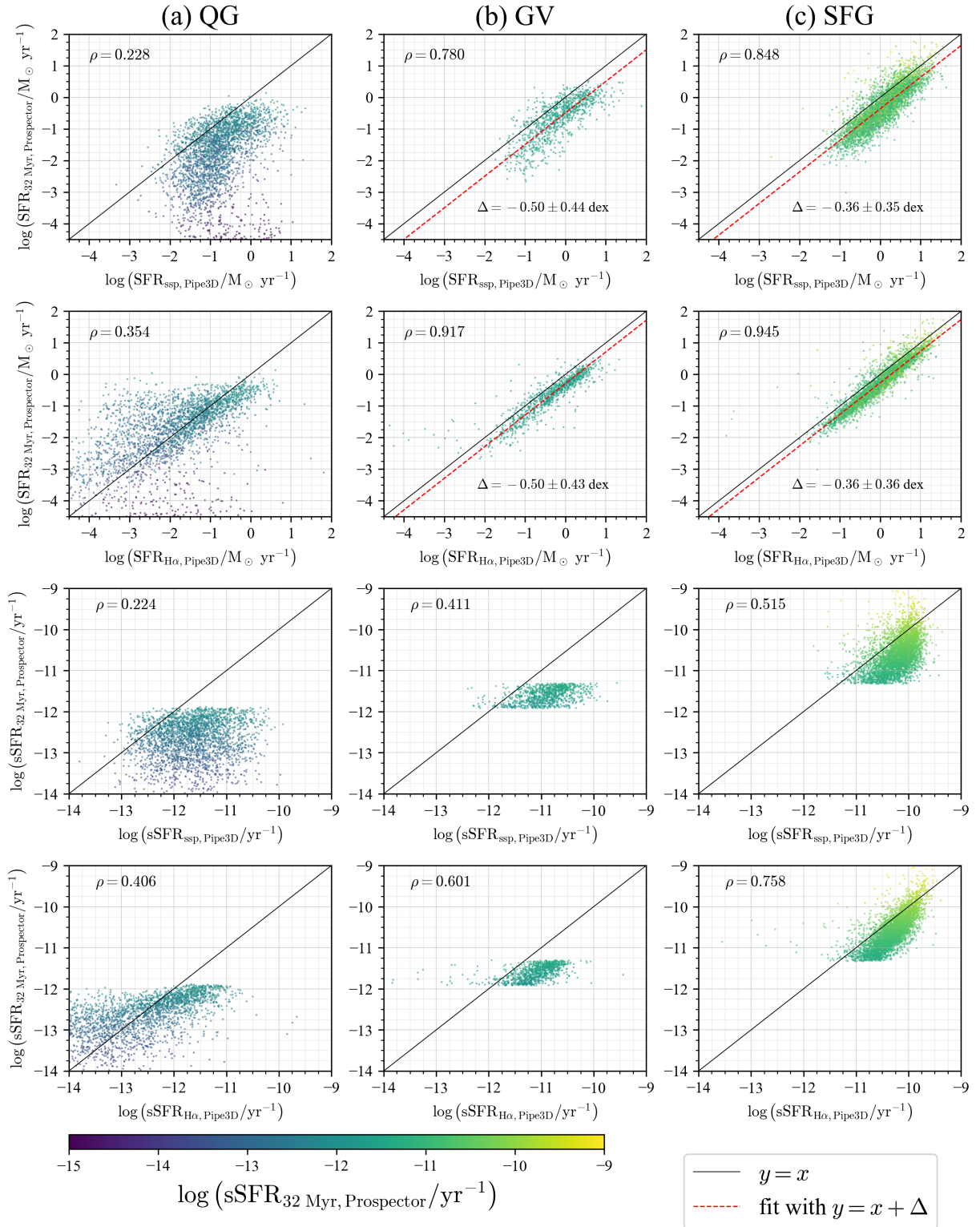


Fig. 21. Comparison of Prospector-estimated SFRs and sSFRs with the Pipe3D catalog values. In lines 1 and 2 (lines 3 and 4), we compare estimated SFRs (sSFRs) in the most recent bin ($t < 32$ Myr) with Pipe3D SFRs (sSFRs) in recent 32 Myr calculated from simple stellar population analysis and H α fluxes, respectively. Rows 1, 2, and 3 are for current QGs, GVs, and SFGs, respectively, classified with sSFRs in the most recent age bin estimated by PROSPECTOR. Spearman's correlation coefficient ρ is shown in the upper left corner of each panel. The solid black lines show the $y = x$ relation. The dashed lines in $\rho > 0.8$ panels show the results of $y = x + \Delta$ fit.

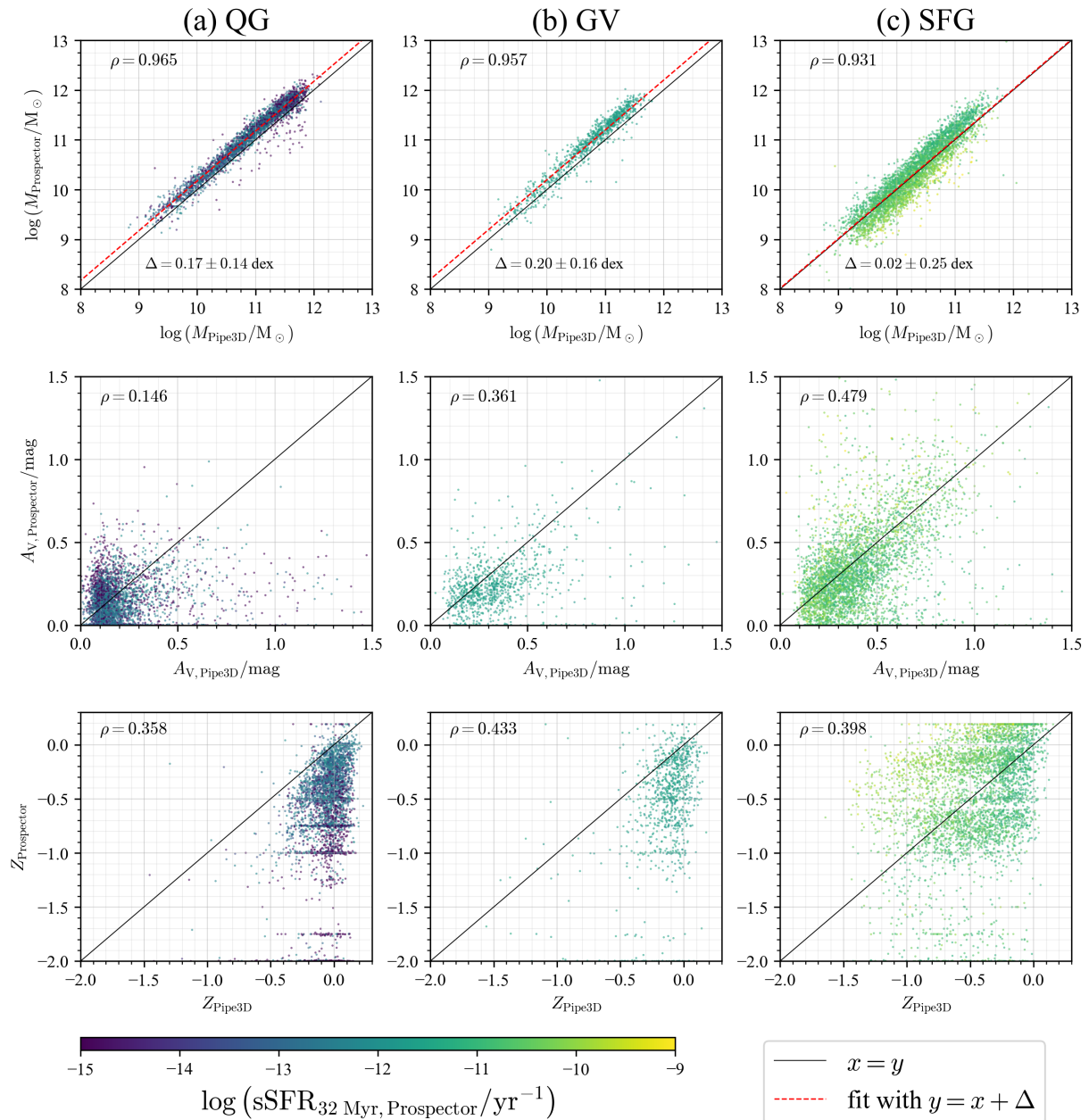


Fig. 22. Same as figure 21, but in lines 1, 2, and 3, we compare estimated M^* , A_V , and Z with Pipe3D values.

and 0.88 for H α -based ones. We note, however, that the SFRs by PROSPECTOR are systematically lower by about 0.6 dex. In contrast, the correlation is very weak for QGs, especially those with $\text{SFR} \lesssim 10^{-1} M_{\odot} \text{ yr}^{-1}$.

Line 1 of figure 22 shows that the stellar masses by PROSPECTOR strongly correlate with those in the Pipe3D catalog ($\log \text{Mass}$), with a Spearman's correlation coefficient calculated for all types of galaxies of $\rho \simeq 0.96$, although PROSPECTOR tends to give slightly higher masses for QGs and GVs. We also find that SFGs with higher sSFR in PROSPECTOR tend to have lower M^* than in the Pipe3D.

In our RG selection, we classify a galaxy into an SFG, GV, or QG at each of the eight age bins using the sSFR and t_H of the bin. Because the redshift range of galaxies in the parent sample is very narrow ($0.01 \leq z \leq 0.15$), the differences in t_H at each age bin among the galaxies are less than $\sim 15\%$. Therefore, comparing PROSPECTOR's sSFRs in the most recent age bin with the Pipe3D's values provides a sensitive test for the validity of our RG selection.

Lines 3 and 4 of figure 21 compare sSFRs for each galaxy type. For the whole sample, we obtain a high Spearman's correlation coefficient of $\rho \simeq 0.84$ (vs. SSP-based sSFR) and 0.91 (H α -based sSFR). However, as seen from the figure, the correlation in a given galaxy type is not so strong, being weaker than that for SFR and M^* . This is mainly because the classification of SFGs, GVs, and QGs is based on sSFR estimated by PROSPECTOR; thus, the distribution in each panel has a cutoff at an sSFR.

Line 2 of figure 22 shows that the A_V estimated with PROSPECTOR are weakly correlated with those from the Pipe3D catalog ($A_{V_ssp_Re}$) with a Spearman's correlation coefficient (for all galaxies) of $\rho \simeq 0.48$. The correlation is weakest for QGs. Similarly, we find a very weak correlation for Z ($ZH_LW_Re_fit$ in Pipe3D) in line 3 of figure 22.

In summary, the values of SFR, M^* , and sSFR by PROSPECTOR correlate strongly with those from the Pipe3D catalog despite the presence of systematic offsets. Therefore, we conclude that our results are reliable enough to select RGs. The criteria for RG selection are based solely on PROSPECTOR's outputs. This means that the systematic offsets from Pipe3D's values will not significantly affect our classification.

References

- Abdurro'uf et al. 2022, ApJS, 259, 35
 Aihara, H., et al. 2022, PASJ, 74, 247
 Akhshik, M., et al. 2021, ApJL, 907, L8
 Alarcon, A., Hearin, A. P., Becker, M. R., & Chaves-Montero, J. 2022, MNRAS, 518, 562
 Anghoipo, J., Ferreras, I., & Silk, J. 2020, MNRAS, 495, 2720
 Behroozi, P., Wechsler R. H., Hearin, A. P., & Conroy, C. 2019, MNRAS, 488, 3143
 Belfiore, F., et al. 2019, AJ, 158, 160
 Belli, S., et al. 2017, ApJL, 841, L6
 Bertschinger, E. 1985, ApJS, 58, 39
 Blanton, M. R., et al. 2017, AJ, 154, 28
 Bundy, K., et al. 2015, ApJ, 798, 7
 Byler, N., Dalcanton, J. J., Conroy, C., & Johnson, B. D. 2017, ApJ, 840, 44
 Calzetti, D., Armus, L., Bohlin, R. C., Kinney, A. L., Koornneef, J., & Storchi-Bergmann, T. 2000, ApJ, 533, 682
 Carnall, A. C., et al. 2019, MNRAS, 490, 417
 Chabrier, G. 2003, PASP, 115, 763
 Charlot, S., & Fall, S. M. 2000, ApJ, 539, 718
 Chauke, P., et al. 2019, ApJ, 877, 48
 Cid Fernandes, R., et al. 2005, MNRAS, 358, 363
 Cleland, C., & McGee, D. L. 2021, MNRAS, 500, 590
 Comerford, J. M., et al. 2020, AJ, 901, 159
 Conroy, C., Gunn, J. E., & White, M. 2009, AJ, 699, 486
 Conroy, C., & Gunn, J. E. 2010, AJ, 712, 833
 Davidzon, I., et al. 2017, A&A, 605, A70
 Diaz, J., Bekki, K., Forbes, D. A., Couch, W. J., Drinkwater, M. J., & Deeley, S. 2018, MNRAS, 477, 2030
 Dome, T., Tacchella, S., Fialkov, A., Dekel, A., Ginzburg, O., Lapiner, S., & Looser, T. J. 2023, arXiv e-prints, arXiv:2305.07066
 Domínguez Sánchez, H., Margalef, B., Bernardi, M., & Huertas-Company, M. 2022, MNRAS, 509, 4024
 Donas, J., et al. 2007, ApJS, 173, 597
 Drory, N., et al. 2015, AJ, 149, 77
 Dye, S. 2008, MNRAS, 389, 1293
 Elbaz, D., et al. 2007, A&A, 468, 33
 Faber, S. M., et al. 2007, ApJ, 665, 265
 Feldmann, R. 2017, MNRASLett., 470, L59
 Ferland, G. J., Korista, K. T., Verner, D. A., Ferguson, J. W., Kingdon, J. B., & Verner, E. M. 1998, PASP, 110, 761
 Ferland, G. J., et al. 2013, *Revista Mexicana de Astronomía y Astrofísica*, 49, 137
 Fudamoto, Y., Inoue, A. K., & Sugahara, Y. 2022, ApJL, 938, L24
 Giménez-Arteaga, C., et al. 2023, ApJ, 948, 126
 Gobat, R., et al. 2017, A&A, 599, A95
 Goddard, D., et al. 2017, MNRAS, 466, 4731
 Gunn, J. E., et al. 2006, AJ, 131, 2332
 Hao, C.-N., Shi, Y., Chen, Y., Xia, X., Gu, Q., Guo, R., Yu, X., & Li, S. 2019, ApJL, 883, L36
 Hinshaw, G., et al. 2013, ApJS, 208, 19
 Hogg, D. W., Bovy, J., & Lang, D. 2010, arXiv e-prints, arXiv:1008.4686
 Ilbert O., et al. 2013, A&A, 556, 19
 Johnson, B. D., Leja, J., Conroy, C., & Speagle, J. S. 2021, ApJS, 254, 22
 Kaviraj, S., et al. 2007, ApJS, 173, 619
 Kaviraj, S., Peirani, S., Khochfar, S., Silk, J., & Kay, S. 2009, MNRAS, 394, 1713

- Kriek, M., & Conroy, C. 2013, *ApJL*, 775, L16
- Lacerda, E. A. D., Sánchez, S. F., Mejía-Narváez, A., Camps-Fariña, A., Espinosa-Ponce, C., Barrera-Ballesteros, J. K., Ibarra-Medel, H., & Lugo-Aranda, A. Z. 2022, *NewA*, 97, 101895
- Lang, D., Hogg, D. W., & Schlegel, D. J. 2016, *AJ*, 151, 36
- Law, D. R., et al. 2016, *AJ*, 152, 83
- Law, D. R., et al. 2021, *AJ*, 161, 52
- Leja, J., Johnson, B. D., Conroy, C., van Dokkum, P. G., & Byler, N. 2017, 837, 170
- Leja, J., Johnson, B. D., Conroy, C., & van Dokkum, P. 2018, *ApJ*, 854, 62
- Leja, J., Carnall, A. C., Johnson, B. D., Conroy, C., & Speagle, J. S. 2019, *ApJ*, 876, 3
- Liivamägi, L. J., Tempel, E., and Saar, E. 2012, *A&A*, 539, 80
- Looser, J. T., et al. 2023a, arXiv e-prints, arXiv:2302.14155
- Looser, J. T., et al. 2023b, arXiv e-prints, arXiv:2306.02470
- Lower, S., Narayanan, D., Leja, J., Johnson, B. D., Conroy, C., & Davé, R. 2020, *ApJ*, 904, 33
- Lupton, R., Blanton, M. R., Fekete, G., Hogg, D. W., O'Mullane, W., Szalay, A., & Wherry, N. 2004, *The Publications of the Astronomical Society of the Pacific*, 116, 133
- Madau, P., & Dickinson, M. 2014, *ARA&A*, 52, 415
- Mancini, C., et al. 2019, *MNRAS*, 489, 1265
- Mapelli, M., Rampazzo, R., & Marino, A. 2015, *A&A*, 575, 16
- Maraston, C., Pforr, J., Renzini, A., Daddi, E., Dickinson, M., Cimatti, A., & Tonini, C. 2010, *MNRAS*, 407, 830
- Martín-Navarro, I., Shankar, F., & Mezcua, M. 2022, *MNRAS Lett.*, 513, 10
- Muzzin, A., et al. 2013, *ApJ*, 777, 18
- Narayanan, D., et al., 2023, arXiv e-prints, arXiv:2306.10118
- Nelson, D., et al. 2018, *MNRAS*, 475, 624
- Noeske, K. G., et al. 2007, *ApJ*, 660, 43
- Noll, S., Burgarella, D., Giovannoli, E., Buat, V., Marcellac, D., & Muñoz-Mateos, J. C. 2009, *A&A*, 507, 1793
- Ocvirk, P., Pichon, C., Lançon, A., & Thiébaud, E. 2006, *MNRAS*, 365, 46
- Pandya, V., et al. 2017, *MNRAS*, 472, 2054
- Parikh, T., et al. 2018, *MNRAS*, 477, 3954
- Park, M., et al. 2022, *MNRAS*, 515, 213
- Paspaliaris, E. D., Xilouris, E. M., Nersesian, A., Bianchi, S., Georgantopoulos, I., Masoura, V. A., Magdis, G. E., & Plionis, M. 2023, *A&A*, 669, A11
- Pearson, W. J., et al. 2018, *A&A*, 615, 146
- Peng, Y.-j., et al. 2010, *ApJ*, 721, 193
- Popesso, P., et al. 2023, *MNRAS*, 519, 1526
- Rathore, H., Kumar, K., Mishra, P. K., Wadadekar, Y., & Bait, O. 2022, *MNRAS*, 513, 389
- Renzini, A., & Peng, Y. 2015, *ApJL*, 801, L29
- Rhee, J., Smith, R., Choi, H., Yi, S. K., Jaffé, Y., Candlish, G., & Sánchez-Jánssen, R. 2017, *ApJ*, 843, 128
- Sánchez, S. F., et al. 2016a, *RMxAA*, 52, 21
- Sánchez, S. F., et al. 2016b, *RMxAA*, 52, 171
- Sánchez, S. F., et al. 2018, *RevMex*, 54, 217
- Sánchez, S. F. et al. 2022, *ApJS*, 262, 36
- Salim, S. 2014, *Serbian Astronomical Journal*, 189, 1
- Schawinski, K., et al. 2007, *ApJS*, 173, 512
- Schlafly, E. F., Meisner, A. M., & Green, G. M. 2019, *ApJS*, 240, 30
- Schlegel, D. J., Finkbeiner, D. P., & Davis, M. 1998, *ApJ*, 500, 525
- Shimakawa, R., Tanaka, M., Bottrell, C., Wu, P.-F., Chang, Y.-Y., Toba, Y., & Ali, S. 2022, *PASJ*, 74, 612
- Smee, S. A., et al. 2013, *AJ*, 146, 32
- Sorba, R., & Sawicki, M. 2018, *MNRAS*, 476, 1532
- Speagle, J. S., Steinhardt, C. L., Capak, P. L., & Silverman, J. D. 2014, *ApJS*, 214, 15
- Strait, V., et al., 2023, *ApJL*, 949, L23
- Tacchella, S., et al. 2022, *ApJ*, 926, 134
- Tempel, E., Tago, E., & Liivamägi, L. J. 2012, *A&A*, 540, A106
- Thom, C., et al. 2012, *ApJL*, 758, L41
- Thomas, D., Maraston, C., Schawinski, K., Sarzi, M., & Silk, J. 2010, *MNRAS*, 404, 1775
- Tojeiro, R., Heavens, A. F., Jimenez, R., & Panter, B. 2007, *MNRAS*, 381, 1252
- Tomczak, A. R., et al. 2016, *ApJ*, 817, 118
- Trayford, J. W., Theuns, T., Bower, R. G., Crain, R. A., Lagos, C. d. P., Schaller, M., & Schaye, J. 2016, *MNRAS*, 460, 3925
- Treu, T., et al. 2005 *ApJ*, 633, 174
- van den Bergh, S. 1976, *ApJ*, 206, 883
- Wake, D. A., et al. 2017, *AJ*, 154, 86
- Walcher, J., Groves, B., Budavári, T., & Dale, D. 2011, *Astrophysics and Space Science*, 331, 1
- Weaver, J. R., et al. 2022, arXiv e-prints, arXiv:2212.02512
- Westfall, K. B., et al. 2019, *AJ*, 158, 231
- Whitaker, K. E., van Dokkum, P. G., Brammer, G., & Franx, M. 2012, *ApJL*, 754, 29
- Yan, R., et al. 2016, *AJ*, 152, 197
- Zhang, J., Li, Y., Leja, J., Whitaker, K. E., Nersesian, A., Bezanson, R., & van der Wel, A. 2022, *ApJ*, 952, 6